NORTHWESTERN UNIVERSITY

The Azimuthal Decorrelation of Jets Widely Separated in Rapidity

A DISSERTATION

SUBMITTED TO THE GRADUATE SCHOOL
IN PARTIAL FULFILLMENT OF THE REQUIREMENTS

for the degree

DOCTOR OF PHILOSOPHY

Field of Physics

By
SOON YUNG JUN
EVANSTON, ILLINOIS
June 1997

ABSTRACT

The Azimuthal
Decorrelation of Jets Widely
Separated in Rapidity

SOON YUNG JUN

We study the azimuthal decorrelation between jets with pseudorapidity separation up to six units. The data were accumulated using the DØ detector during the 1994–1995 collider run of the Fermilab Tevatron at $\sqrt{s} = 1.8$ TeV. The data are compared to two parton shower Monte Carlos (HERWIG and PYTHIA) where the leading logarithmic terms are resummed to all orders in α_S, and an analytical prediction using the leading logarithmic BFKL resummation. The final state jets as predicted by parton showering Monte Carlo describes the data well over the entire pseudorapidity range studied. The prediction based on the leading logarithmic BFKL resummation shows too much decorrelation as the rapidity interval increases.

Acknowledgements

I would like to express my deepest appreciation to my thesis advisor, Dave Buchholz, for his excellent guidance, sapient advice, and trust in my work. I must also express my sincere thanks to Mr. BFKL, Terry Heuring who has always guided me for this work from the beginning. I also owe a special gratitude to God Fathers of this analysis, Steve Linn, Stefan Gruenendahl, Seung-Chan Ahn, for their careful supervision and endless discussion. I appreciate every support provided by the Northwestern High Energy Group and the DØ QCD group, especially past and present convener of the QCD group, Jerry Blazey, Bob McCarthy, Nikos Varelas, and Heidi Schellman. I also would like to thank Mrinmoy and Kisuk for their friendship.

My greatest thanks goes to my wife, Seon Hwa Eun. No word will be necessary to describe her love, understanding, being together all these years. Finally I would like to dedicate this work to my parents.

I appreciate the Fermilab Accelerator, Computing, and Research Divisions, and the support staffs at the collaborating institutions for their contributions to the success of this work. I also acknowledge the support of the U.S. Department of Energy, the U.S. National Science Foundation, the Commissariat à L'Energie Atomique in France, the Ministry for Atomic Energy and the Ministry of Science and Technology Policy in Russia, CNPq in Brazil, the Departments of Atomic Energy and Science and Education in India, Colciencias in Colombia, CONACyT in Mexico, the Ministry of Education, Research Foundation and KOSEF in Korea, CONICET and UBACYT in Argentina, and the A.P. Sloan Foundation.

Contents

List of Tables

List of Figures

Chapter 1

Introduction

In the eyes of elementary particle physicists, flavors of nature are up and down, strange and charm, and beauty and truth. Each flavor comes in three colors (Red, Green, and Blue) while the world is invariant under color interchange. Color-anticolor gluons string themselves into structured colorless hadrons. Point-like color singlet leptons join to synthesize spontaneous symmetry breaking under the scalar Higgs fields. A black hole is bald due to the static limit, but a jet is hairy due to color confinement. The quantum world is to be renormalized but running. Antiscreening of hidden color charges gives asymptotic freedom for the strong interaction party.

Quantum Chromodynamics (QCD) is the gauge theory of strong interactions between quarks as mediated by gluons. The central theoretical concept of QCD is color, the three quantum states of a quark. Gauge invariance under color transformation introduces eight massless gluons carrying pairs of color labels. The two most striking features of the theory are color confinement and asymptotic freedom. Color confinement is the fact that no isolated quark or gluon can be seen. Only colorless states are allowed as physical hadrons - combinations of three quarks with different colors (baryons) or of quark-antiquark with color-anticolor pairs (mesons). Asymptotic freedom is a consequence of the theory that the coupling strength between colors decreases at distances short compared to the physical size of the hadron. This enables perturbative techniques to be used to calculate QCD predictions for hard scattering processes involving partons (quarks and gluons) with large momentum transfers (Q).

All applications of perturbative QCD to partonic processes with hadrons in the initial state are based on the factorization theorem [1] in which a general parton model cross section can be factorized into a reaction probability, a calculable partonic cross section, and a hadronization process converting quarks or gluons into hadrons. The hadronization scale, Λ_{QCD}, characterizes physics at long distances where scattered partons split from their parent hadrons (parton distribution functions) and final state partons hadronize (fragmentation functions). The perturbative description of QCD is only valid for $Q^2 >> \Lambda^2{}_{QCD}$ where the running coupling $\alpha_s(Q^2)$ remains small enough for a perturbative treatment. Technically Λ_{QCD} is introduced into the theory by a regularization procedure for divergences in QCD calculations, and is removed by a renormalization procedure for absorbing regularized divergences into the definition of physical quantities by introducing an arbitrary renormalization scale μ. The running of the coupling constant and asymptotic freedom result from the renormalization group equation that expresses the invariance of the physics under changes of the renormalization scale μ. Perturbative calculations are then based on the leading logarithmic approximation (LLA) which includes all leading-log terms in powers of $[\alpha_s^2(Q^2)\ln(Q^2)]^n$ for all n, restricted to $\alpha_s^2(Q^2) << 1$ for convergence.

The reliability of perturbative QCD calculations depends on how well general features of the QCD theory are combined for a particular process in a specific kinematic region as well as how sensitive the LLA is to perturbative expansions of QCD calculations. Nonetheless perturbative QCD calculations beyond a certain fixed order are extremely difficult. By the same token, QCD predictions for multiparton kinematics including the transition regime from perturbative physics at short distances to non-perturbative physics at long distances need challenging working tools. One of the theoretical techniques to describe multiparton (Regge) kinematics is the theory of

Balitsky, Fadin, Kuraev, and Lipatov (BFKL) [2] which describes a gluon-ladder evolution of reggized gluons ordered in rapidity with comparable momenta. The BFKL theory systematically resums leading logarithmic contributions of soft gluon radiation to all orders in α_s.

Recent applications of BFKL theory can be found in exploring the large kinematic region in deep inelastic scattering (DIS) by the electron-proton collider at HERA and in inclusive dijet (two jets) production process by the proton-antiproton ($p\bar{p}$) collider at the Tevatron. The BFKL equation [2] may explain the sharp rise of DIS structure functions at small-x governed by the BFKL pomeron. At the Tevatron, signatures of BFKL dynamics are the rise of the total cross section and jet-jet decorrelation in the inclusive dijet production at large rapidity intervals. This thesis investigates the jet-jet decorrelation in the azimuthal angle on the inclusive dijet production at the Tevatron $p\bar{p}$ collider to probe high order QCD effects in certain kinematic regions of phase space as well as to test the BFKL resummation technique. In the following sections, we briefly review jet physics in hadron-hadron collisions, the motivation of this study, and the inclusive dijet production at large rapidity intervals.

1.1 Jet Physics in Hadron-Hadron Collision

A jet is a spray of particles produced in the hadronization process of a parton (quark or gluon) into hadrons. Jet production caused by color confinement of partons can be predicted with perturbative QCD for processes involving large momentum transfers. For the last two decades, comparisons have been made between perturbative QCD predictions and experimental results involving jets produced in high energy lepton-lepton, lepton-hadron, and hadron-hadron colliders. These comparisons include precision tests for the running of the strong coupling constant (α_s), parton distribution functions, inclusive jet cross sections, jet shape variables and topologies, and many other processes with jets accompanying vector boson and heavy-quark production.

Recently there has been a great deal of interest in multijet and small-x physics as a trigger to explore varieties of jet physics beyond the current frontier of QCD.

Experimentally, jets are defined by algorithms which quantify certain topological features of hadronic energy flow in the final state of scattering processes. Jet cross sections in hadron-hadron collisions have usually been measured in term of the cone algorithm whose main features were specified in an agreement reached at the 1990 Snowmass Workshop [3]. A cone jet consists of all the particles whose momentum vectors lie inside a cone of radius R in $\eta - \phi$ space ($R = \sqrt{\Delta\eta^2 + \Delta\phi^2}$). Here η is pseudorapidity ($\eta = -\ln\tan\theta/2$) and ϕ is the azimuthal angle with respect to the direction of the colliding hadrons. Experimentally the transverse energy (E_T) is used as a kinematic variable which is approximately equivalent to the sum of transverse momentum of all particles belonging to a jet. Detailed features of the cone algorithm used in this thesis will be discussed in Chapter 3.

Jet production at hadron-hadron colliders, as a consequence of the factorization theorem in the parton model, involves many different scales; the center-of-mass energy($\sqrt{s}$), the parton-parton center-of-mass energy($\sqrt{\hat{s}} = \sqrt{x_A x_B s}$) where x_A and x_B are the momentum fractions of the intial partons, the momentum transfer(Q) which is of order of the transverse momentum of the jets in the hard scattering, and the hadronization scale Λ_{QCD}. The effects of Λ_{QCD} are factorized into the parton distribution function or the fragmentation function which can be described semi-empirically. The partonic (hard scattering) cross sections can be calculated through perturbative QCD as an expansion of $\alpha_s \ln(s/Q^2)$. Subsequent parton evolution of scattered partons emitting gluons, known as parton showering, generally describes higher order hard scattering processes while fixed order perturbative calculations only include exact terms in the expansion of $\alpha_s \ln(s/Q^2)$ to a given accuracy. The hadronization process following the parton shower is responsible for the regrouping of quarks and antiquarks produced by emitted gluons into a collimated spray of hadrons called jets. Therefore, the general parton model jet cross sections can be represented

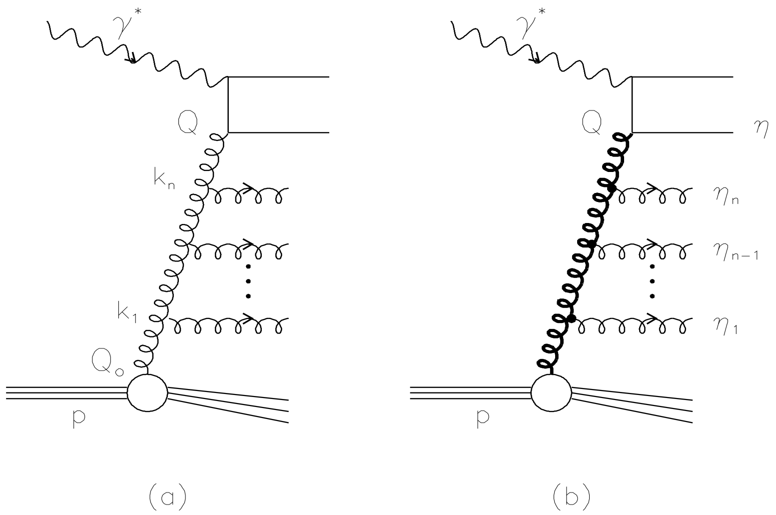

Figure 1.1: The evolution of parton density in the deep inelastic scattering (DIS). (a) DGLAP - a strong $k_\perp$ ordering ($Q > k_{\perp n} > ... > k_{\perp 1} > Q_o$). (b) BFKL - a strong rapidity ordering with comparable size of $k_\perp$ ($\eta_1 > \eta_2 > ... > \eta_n > \eta$); $k_\perp \simeq k_{\perp i}$.

as a convolution of perturbative hard scattering cross sections, and non-perturbative parton distribution functions and hadronization processes.

The parton distribution function describes the probability of a parton carrying a fractional momenta in a hadron. It is expected to be universal but should be measured in other processes at fixed scales. For other values of the factorization scale μ, it can be calculated via the evolution of parton densities that has been described by both the Altarelli, Parisi, Gribov, Lipatov, Dokshitzer (DGLAP) equation [4] and the BFKL equation. The DGLAP equation resums the collinear logarithms ($\alpha_s \ln Q^2$) in the evolution at a given loop-accuracy as determined by Altarelli-Parisi splitting functions that describe a generalized parton evolution along a space-like cascade in which the successive transverse momenta are strongly ordered as shown in figure 1.1.(a). The DGLAP equation usually describes a parton evolution along Q^2

with a fixed momentum fraction x. On the other hand, the BFKL equation generally resums the large leading ($\alpha_s \ln x$) contribution in the small-x region ($x << 10^{-2}$). BFKL evolution generally represents a strong ordering of emitted gluons in x, or rapidity, but with comparable momenta as shown in figure 1.1.(b).

Perturbative QCD calculations have been worked out primarily at fixed order of α_s and in the kinematic region involving one invariant scale, $Q \approx \sqrt{\hat{s}} \approx \sqrt{s}$. The current state-of-the-art of jet physics at hadron colliders is reasonably well described by next-to-leading order (NLO) QCD parton-level calculations [5, 6]. These calculations combine the one-loop $2 \rightarrow 2$ virtual correction with the tree-level $2 \rightarrow 3$ parton scattering. Examples of Feynman diagrams representing a parton-parton scattering with the one-loop and the tree level are shown in figure 1.2. The comparison between NLO QCD calculations and Tevatron data for jet inclusive cross sections are in good agreement within the theoretical uncertainties of the renormalization scale ($\sim 10\%$), the parton distribution functions ($\sim 20\%$), clustering algorithms ($\sim 5\%$), and the experimental errors ($\sim 20 \sim 40\%$ with E_T dependence) [7].

Along with many successes involving just one large energy scale, there have been efforts to probe higher order effects involving multi jet production and alternate scales. Since it is prohibitively difficult to make exact calculations for a general multiparton process, calculations have been made via Monte Carlo simulation based on the LLA. Generally high order QCD effects are sensitive to parton evolution schemes depending on the amount of soft radiation in the parton showering process. Another theoretical technique to handle multiparton kinematics over large rapidity and small-x region is BFKL resummation which resums a certain type of soft gluon radiation to all orders in α_s using LLA. In general, the interpretation of higher order processes is complicated by the presence of many other processes, such as: 1) effects of underlying-event produced by the soft interaction of the spectator partons in the colliding hadrons, 2) jet merging in the case of overlapping cones depending upon the particular jet finding algorithm used, and 3) the size of non-perturbative fragmentation contributions due

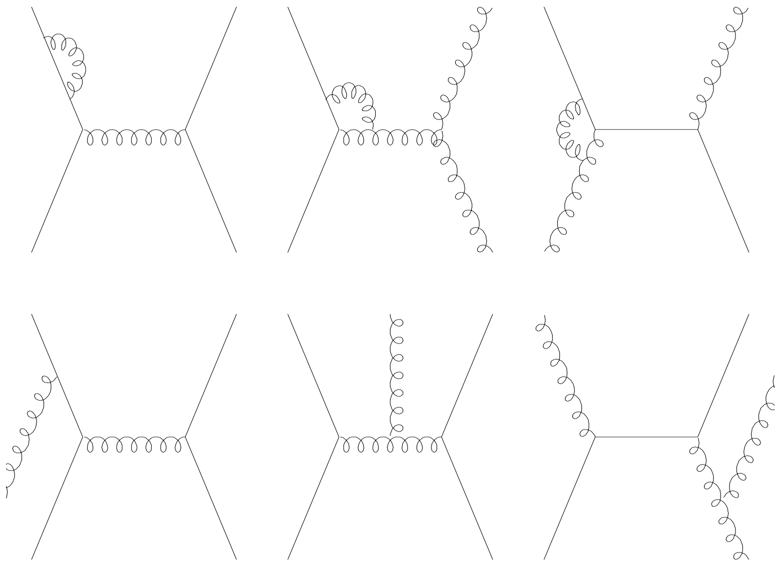

Figure 1.2: Examples of next-to-leading order parton-parton scattering with one-loop corrections and the tree level subprocesses. The straight lines represent quarks and the curly lines gluons.

to the confinement of partons. This thesis searches for some high order QCD effects and tests of BFKL resummation in the semi-hard region ($Q >> \sqrt{s}$) at the Fermilab Tevatron collider.

1.2 Quest for the Perturbative QCD Pomeron

The perturbative QCD pomeron (BFKL pomeron) exchange is defined as the exchange of a two gluon ladder with the quantum numbers of the vacuum in a color singlet configuration [2]. This is the phenomenon obtained by resumming a certain type of soft gluon emission to all orders in the leading logarithmic approximation using the BFKL equation. The total cross section for one-gluon exchange in the $\hat{t}$ channel can be related via the optical theorem to the color singlet solution of the BFKL equation. The exponential growth of the dijet inclusive cross section with increasing rapidity interval between the tagging jets at the extremes of rapidity was originally proposed as an experimental signature of the QCD perturbative pomeron [8]. At a fixed collider energy, the azimuthal decorrelation of jets widely separated in rapidity was suggested as an alternative approach to search for the BFKL dynamics [9, 10]. The broadening of the azimuthal angle difference distribution with increasing dijet rapidity interval can be quantified by using BFKL dynamics. The first measurement of the azimuthal decorrelation between jets with pseudorapidity separation up to five units was previously reported by the DØ collaboration [11].

The earlier DØ paper reported results on decorrelation of jets with asymmetric E_T thresholds - 20 GeV and 50 GeV on the tagging jet E_T. The thresholds were set to ensure full trigger efficiency (50 GeV) and jet reconstruction efficiency (20 GeV) for the sample used. The asymmetric E_T thresholds might emphasize a kinematic imbalance of the inclusive dijet production. It has also been shown that lower symmetric thresholds yield more sensitive BFKL effects [9] as well as probe a new kinematic region of phase space. We have extended the previous measurement of the azimuthal decorrelation by employing a lower, symmetric jet E_T threshold cut (20 GeV) and allowing a pseudorapidity separation of up to six units with data collected by the DØ detector during the 1994-1995 collider run. Results from data are compared to an analytical prediction based on the leading logarithmic BFKL resummation [12], and the parton showering Monte Carlos HERWIG [13], PYTHIA [14], and ISAJET [15], in which higher order effects are approximated by the parton shower approach which is superimposed on the leading order QCD 2 to 2 parton process. In the following subsection, we briefly review dijet production at large rapidity intervals outlined in many references [8, 16, 17].

1.3 Dijet Production at Large Rapidity Intervals

As the energy of hadron-hadron colliders increases, there may be kinematic regions involving more than one relevant energy scale. At the Tevatron $p\bar{p}$ collider with $\sqrt{s} =$ 1800 GeV the semihard region of kinematic phase space, where $\Lambda_{QCD} \ll Q \ll \sqrt{s}$, is accessible. In this region, the large logarithm can be written as

$$\ln \frac{s}{Q^2} = \ln \frac{1}{x_p} + \ln \frac{\hat{s}}{Q^2} + \ln \frac{1}{x_{\bar{p}}}. \tag{1.1}$$

The $1/x$ logarithms appear in the evolution of the parton densities and $\ln(\hat{s}/Q^2)$ parameterizes the hard scattering cross section. Requiring that the parton momentum fractions, x_p and $x_{\bar{p}}$, are sufficiently large to avoid complication with the small-x behavior of parton distribution functions, the large logarithms $\ln(\hat{s}/Q^2)$ factorize entirely into the partonic subprocess cross section. Then the logarithms, which are of the size of the rapidity interval in the scattering process, can be resummed using the techniques of BFKL.

Consider a description of the inclusive dijet process in $p\bar{p}$ collisions at the semihard region of kinematic space with Q^2 as a typical momentum scale in the event ($Q^2 \approx p_{1\perp}p_{2\perp}$). Jets are ordered in rapidity ($\eta_1 \gg ... \gg \eta_2$) and have comparable transverse momentum of size Q ($p_{i\perp} \simeq Q$). If two tagging jets are chosen at the extremes of rapidity, then their rapidity interval is

$$\Delta\eta = \eta_1 - \eta_2 \quad \approx \quad \ln(\frac{\hat{s}}{Q^2}). \tag{1.2}$$

All hadron activities in the rapidity interval between two tagging jets are called minijets. Other relevant parameters in the event are the relative azimuthal angle $\Delta\phi = \phi_1 - \phi_2$ and the rapidity boost $\overline{\eta} = (\eta_1 + \eta_2)/2$ of the two jets. The cross section in the semihard region can be written as follow [16]:

$$\frac{d\sigma}{dp_{1\perp}^2 dp_{2\perp}^2 d\Delta\phi d\Delta\eta d\overline{\eta}} = \sum_{ij} x_p x_{\bar{p}} f_{i/p}(x_p, \mu^2) f_{j/\bar{p}}(x_{\bar{p}}, \mu^2) \frac{d\hat{\sigma}_{ij}}{dp_{1\perp}^2 dp_{2\perp}^2 d\Delta\phi}, \tag{1.3}$$

where $f_{i(j)}$ is the parton distribution function of flavor $i(j) = q, \overline{q}$ and g inside the initial hadron $p(\bar{p})$. The hard scattering cross section, $\hat{\sigma}_{ij}$, contains all information of multiparton kinematics including all minijets and can be expressed via the solution of the BFKL equation.

In the exact leading order (Born level) calculation, two and only two jets are produced back-to-back in azimuthal angle balancing their transverse momentum. In the next-to-leading order calculation, one additional radiation is allowed besides the two tagging jets, which may force a change in the back-to-back configuration. The correlation will eventually disappear as more and more soft radiation between two tagging jets is allowed in higher order processes. Many Monte Carlo event generators implement parton showering schemes based on the DGLAP evolution and fragmentation models to approximate calculations to all orders. Recently Mueller and Navelet, and many others have shown that the inclusive dijet production at large rapidity can be handled using the BFKL equation following by multiparton kinematics [8, 9, 16].

Using a multigluon amplitude where the rapidity interval between the tagging jets is filled with gluons, ordered in rapidity, the BFKL theory systematically resums the leading logarithmic contributions of large $\Delta\eta$ or equivalently $\ln(\hat{s}/Q^2)$ in the partonic process. The partonic cross section for the production of two gluons, resummed to all orders of $\alpha_s \ln(\hat{s}/p_\perp^2)$, is written as the convolution of the inverse Laplace transformation of the singlet solution of the BFKL equation, $f(p_{1\perp}, p_{2\perp}, \Delta\eta)$, with the parton production vertices on each side of the rapidity interval

$$\frac{d\hat{\sigma}_{gg}}{dp_{1\perp}^2 dp_{2\perp}^2} = [\frac{C_A \alpha_s}{p_{1\perp}^2}] f(p_{1\perp}, p_{2\perp}, \Delta\eta) [\frac{C_A \alpha_s}{p_{2\perp}^2}], \tag{1.4}$$

where $C_A = 3$ is the Casimir operator of the adjoint representation. The BFKL kernel $f(p_{1\perp}, p_{2\perp}, \Delta\eta)$ describes the gluon-ladder evolution in LLA of $\ln(\hat{s}/Q^2)$ and contain all the information about the hard scattering separated from the parton distribution functions by using the factorization theorem. The explicit expression of $f(p_{1\perp}, p_{2\perp}, \Delta\eta)$ can be obtained by the eigenvalues of the homogenous BFKL solution.

The approximate leading logarithmic cross section can be obtained by considering the leading contribution in an expansion of the eigenvalues of the homogenous BFKL equation,

$$\frac{d\hat{\sigma}_{gg}}{dp_{1\perp}^2 dp_{2\perp}^2 d\Delta\phi} = \frac{C_A^2 {\alpha_s}^2}{8p_{1\perp}^3 p_{2\perp}^3} \frac{e^{(\alpha_p-1)\Delta\eta}}{\sqrt{B\pi\Delta\eta}} e^{-\frac{\log^2(p_{1\perp}^2/p_{2\perp}^2)}{4B\Delta\eta}}, \tag{1.5}$$

where $\alpha_p - 1 = 12\alpha_s \ln 2/\pi \approx 0.5$ and $B = 14C_A\alpha_s\zeta(3)/\pi$. It shows a diffusion pattern with rate $\log^2(p_{1\perp}^2/p_{2\perp}^2) \sim \sqrt{\Delta\eta}$, i.e., it has the form of a Gaussian distribution in $\log^2(p_{1\perp}^2/p_{2\perp}^2)$ with a peak positioned where the partons are balanced in $p_\perp$ and with a width growing with $\Delta\eta$. This diffusion pattern is directly related to the $p_\perp$-decorrelation pattern as the rapidity interval increases. Similarly, the asymptotic value of the total cross section at large rapidity intervals is given by

$$\hat{\sigma}_{gg} = \frac{\pi C_A^2 {\alpha_s}^2}{p_{\perp min}^2} \frac{e^{(\alpha_p-1)\Delta\eta}}{\sqrt{\pi B\Delta\eta}} \tag{1.6}$$

for a parton transverse momenta above a cutoff $p_{\perp min}^2$. The predicted exponential growth of the dijet inclusive cross section with the rapidity interval $\Delta\eta$ is due to the production of the minijets governed by the BFKL pomeron.

The growth rate of the total cross section due to radiative corrections is defined as the K-factor by dividing Eq.(1.6) by the Born cross section above the cutoff $p_{\perp min}^2$ at the large Δy limit:

$$K \simeq \frac{2e^{(\alpha_p-1)\Delta\eta}}{\sqrt{\pi B\Delta\eta}} \tag{1.7}$$

with $\Delta\eta = \ln(\hat{s}/p_{\perp min}^2)$. Mueller and Navelet [8] have proposed measuring dijet production at fixed x's and different $\Delta\eta$ to disentangle the dynamic rise of the dijet cross section from kinematic variations induced by the parton densities. In the large $\Delta\eta$ limit, the K-factor of dijet production at fixed x's coincides with the K-factor of the total cross section. In a hadron-hadron collider with a variable center-of-mass energy, the growth rate of dijet production at fixed parton momentum fractions may be related to the growth of the total parton cross section governed by the BFKL pomeron. Mueller has suggested measuring the ratio of inclusive dijet cross sections for two different center of mass energies with fixed x's to extract α_p [18];

$$\frac{\sigma_1(x_1, x_2, s_1, \Delta\eta_1)}{\sigma_2(x_1, x_2, s_2, \Delta\eta_2)} = \sqrt{\frac{\Delta\eta_2}{\Delta\eta_1}} e^{(\alpha_p - 1)\ln(\frac{s_1}{s_2})} \tag{1.8}$$

at the Tevatron where $s_1 = 1800$ GeV and $s_2 = 630$ GeV .

As an alternative probe of BFKL dynamics at a fixed collider energy, the jet-jet decorrelation in the transverse momentum and azimuthal angle was proposed by Del Duca and Schmidt [16, 10], and independently Stirling [9]. Minijets produced in the rapidity interval will cause the tagged jets to become uncorrelated. In the asymptotic limit of large rapidities, the correlations between the two gluons(jets) are washed out by the random walk in transverse momentum space of the gluons exchanged in the $\hat{t}$ channel. Theoretical calculations have been performed to predict $p_\perp$ decorrelation [16] and ϕ decorrelation [9, 10]. Measuring the quadruple cross section $d^4\sigma/dp_{1\perp}dp_{2\perp}d\Delta\eta d\bar{\eta}$ and the triple cross section $d^3\sigma/d\Delta\eta d\bar{\eta}d\Delta\phi$ give the qualitative signatures of $p_\perp$ and ϕ decorrelation, respectively. As an example, the flattening of the $\Delta\phi$ distribution with increasing dijet rapidity interval over a fixed $\bar{\eta}$ range is an expected characteristic feature of the BFKL behaviour.

A more convenient quantity to test the BFKL picture of the ϕ decorrelation is the moments of the azimuthal angle difference, defined by

$$< \cos n(\Delta\phi - \pi) >= \frac{\int_0^{2\pi} d\phi \cos n(\Delta\phi - \pi)(d\sigma/d\Delta\eta d\Delta\phi)}{\int_0^{2\pi} d\phi(d\sigma/d\Delta\eta d\Delta\phi)}. \tag{1.9}$$

At the Born level the $\Delta\phi$ distribution at $\Delta\phi = \pi$ is expected to be a δ-function which would make all moments be equal to unity. For a flat distribution in $\Delta\phi$ all of the moments will equal zero for $n \geq 1$. Thus the difference of the moments from unity as a function of $\Delta\eta$ is a good measure of the decorrelation in $\Delta\phi$. In the following chapters the measurement of $< \cos(\Delta\phi - \pi) >$ as a function of $\Delta\eta$ (up to $\Delta\eta = 6$) with $p_\perp \geq 20$ GeV will be described with experimental systematics included.

Chapter 2

The DØ Detector

2.1 Overview

The DØ detector is a general purpose collider detector which was optimized for the detection of electrons, muons, jets and missing transverse momentum. Located at the DØ collision hall at Fermilab, the detector consists of three major systems; central tracking, calorimeter, and muon systems as shown in figure 2.1. Characteristic features of the detector are the following: 1) compact non-magnetic tracking with good spatial resolution, 2) hermetic, finely segmented calorimeter based on the detection of ionization in liquid argon, and 3) thick magnetized iron absorbers for muon detection.

The compact non-magnetic central tracking system consists of the Vertex Drift Chamber, the Transition Radiation Detector, and the Central Drift Chamber and two Forward Drift Chambers. Central tracking provides track information for charged particles and the vertex position of the interaction. The uranium liquid argon sampling calorimeter system consists of the Central Calorimeter, the two mirror-image End Calorimeters along with the Intercryostat Detectors, the Massless Gaps, and the Cryogenic System. Single particle energy resolutions are $15\%/\sqrt{E}$ and $50\%/\sqrt{E}$ (E in GeV) for electrons and pions, respectively. Fine segmentation ($\Delta\eta \times \Delta\phi = 0.1 \times 0.1$) of

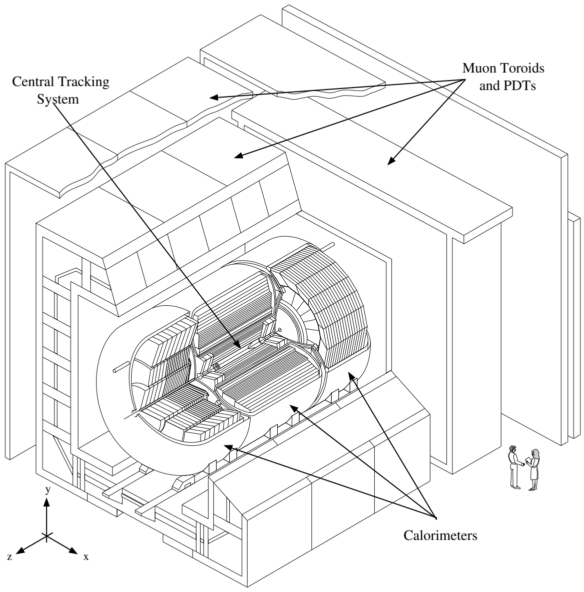

Figure 2.1: The DØ detector.

the calorimeter facilitates identifying electromagnetic and hadronic showers and measuring the position of jets as well as electrons and photons. The hermetic and thick calorimeter also facilitates measuring the missing transverse energy ($\not\!\!E_T$). The muon detection system consists of five separate solid-iron toroidal magnets surrounded by three layers of proportional drift tube chambers to measure charged track coordinates down to $\approx 3^o$ with respect to the beam. The primary purpose of the muon system is to identify muons and to determine their trajectories and momenta combined with information provided by the central tracking. A detailed description along with a summary of relevant properties of all the DØ detector subsystems is given elsewhere [19].

The DØ coordinate system is a right-handed system in which the z-axis is colinear with the proton direction and the y-axis is vertically upward. The angles θ and ϕ are respectively the polar and azimuthal angles with respect to $+\hat{z}$. The pseudorapidity, $\eta \equiv -\ln\tan(\theta/2)$, is commonly used in place of θ and is also an approximation for the rapidity variable y which is valid for most of the regions of interest in this experiment.

2.2 The Detector for Jet Analysis

In this section the functional descriptions of those portions of the detector used for jet analysis are briefly summarized. Important features of the jet identification algorithm will be discussed in the next chapter.

2.2.1 Presence of Inelastic Collision

The presence of an inelastic collision is indicated by two hodoscope arrays of scintillation counters mounted on the front surface of both of End Calorimeters. The counters, with time resolutions of typically $100 \sim 150$ ps, are read out through photomultiplier tubes. A coincidence of two counters indicates a non-diffractive inelastic collision (Level 0 Trigger). The difference in arrival time for particles hitting the two detectors determines the z coordinate of the primary interaction point. A cut $|z_{vertex}| < 100$ cm is made to separate beam-beam interactions from beam-gas and beam-halo events. The efficiency in detecting non-diffractive inelastic collisions is greater than 99%. The rms deviation of the time difference is also used to flag events with multiple interactions.

2.2.2 Vertex Measurement

Finding a primary vertex is very important to reconstruct the four vectors of jets as well as other physical objects such as electrons, direct photons, and muons. This measurement is done primarily by the Vertex Chamber (VTX) and the Cental Detector Chamber (CDC), shown in figure 2.2. The CDC consists of four cylindrical layers of drift cells and covers roughly the pseudorapidity region $|\eta| < 1.2$. The CDC forms a concentric cylinder around the Transition Radiation Detector (TRD) and provides a good pointer to the Central Calorimeter energy cluster. The z coordinate comes from the time difference between two signals collected from both ends of the delay lines induced by the nearest anode sense wires. The x-y position comes by measuring

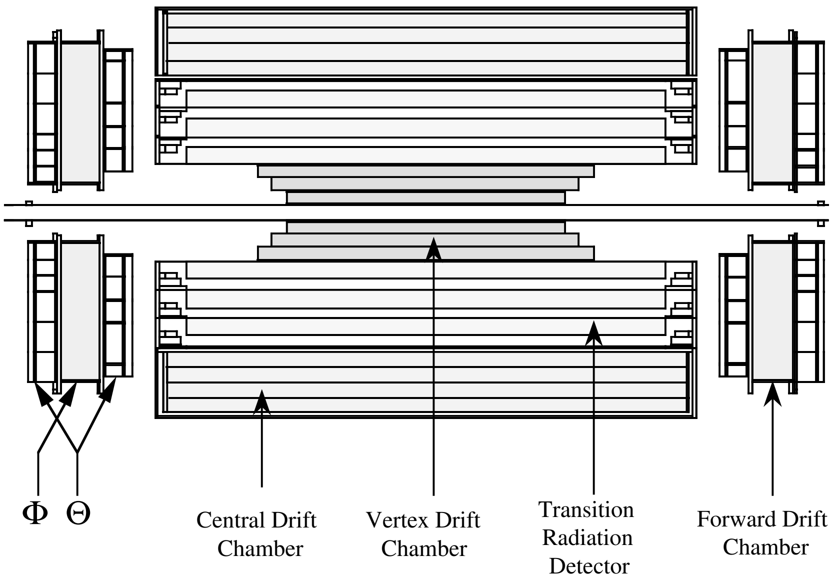

Figure 2.2: Side view of the DØ tracking detectors.

the drift time and knowing the location of the sense wire which find hits associated with charged tracks.

For a forward event, which has no activity in the central region, the Forward Drift Chamber (FDC) full tracking is done automatically. The FDC tracking is not normally done for vertex finding except for events with little or no activity in the central region. The FDC extends the θ coverage for charged particles down to $\theta \approx 5^o$ with respect to both emerging beams. For these special events, the vertex position is determined by only FDC tracks. A procedure similar to that used for the CDC is then used to determine the vertex. Only one vertex is reconstructed using FDC tracks.

The VTX is also generally used for primary vertex identification. The three concentric cylindrical layers of drift cells are designed to measure charged tracks in the vicinity of the interaction region to provide information in reconstructing the interaction vertex. The z vertex is obtained by comparing the integrated pulse areas from both ends of resistive sense wires in each drift cell.

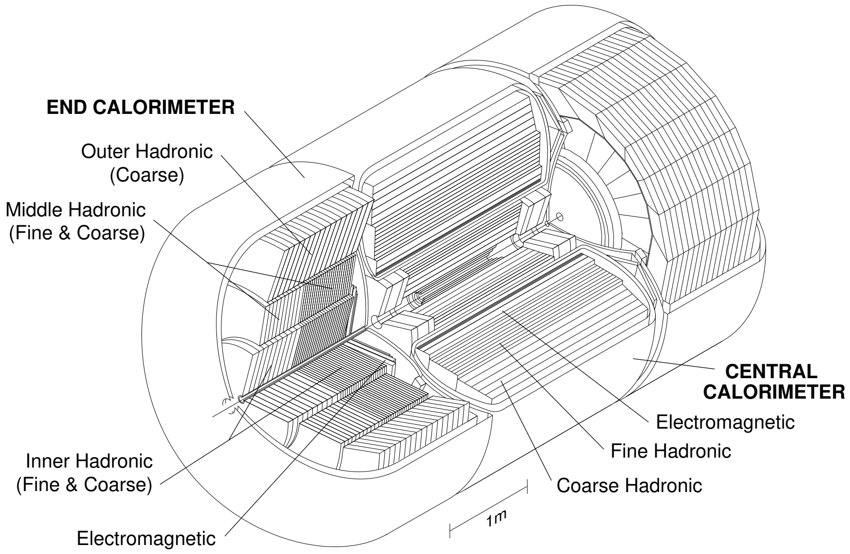

Figure 2.3: The DØ calorimeters.

2.2.3 Calorimeter Readout

The DØ calorimeters, shown in figure 2.3, are sampling calorimeters that sample only a known fraction of the energy lost by a particle. The main features of the DØ calorimeter relevant for jet physics are its fine transverse segmentation ($\Delta\eta \times \Delta\phi = 0.1 \times 0.1$) and large coverage in pseudorapidity ($|\eta| < 4.5$). The Central Calorimeter covers $|\eta| < 1.2$ and the two End Calorimeters cover $1.1 < |\eta| < 4.5$. Each calorimeter consists of three distinct types of calorimeter modules: an electromagnetic section with uranium absorber plates, a fine hadronic section with uranium plates and a coarse hadronic section with copper or stainless steel plates.

The transverse size of the cells were chosen to be comparable to the transverse size of showers: $1 \sim 2$ cm for electromagnetic showers and ~ 10 cm for hadronic showers. The variables more directly useful for physics are $\Delta\eta$ and $\Delta\phi$; the scale is set by the typical size of parton jets, $\Delta R = \sqrt{\Delta\eta^2 + \Delta\phi^2} \sim 0.5$. Segmentation finer than this is useful in probing the structure within jets. The side view of the DØ calorimeter

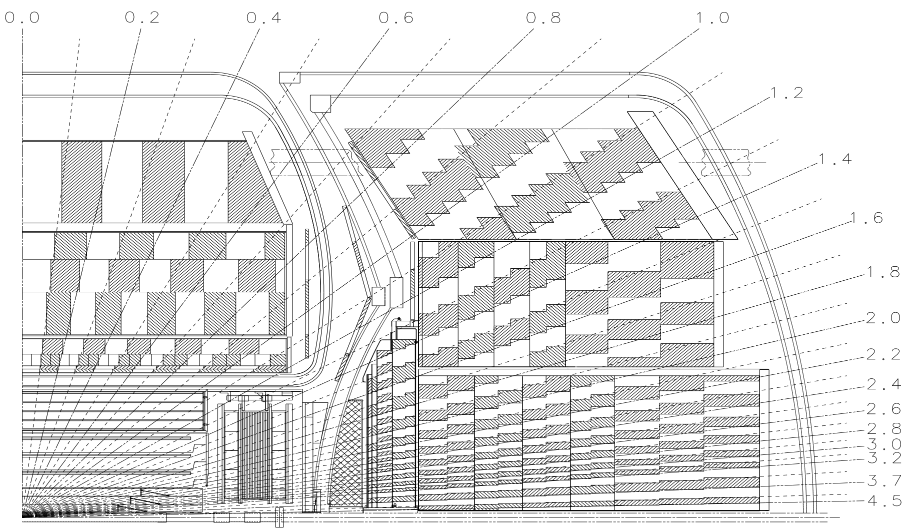

Figure 2.4: Side view of the DØ calorimeter system with its segmentation pattern.

systems with segmentation pattern is shown in figure 2.4. The longitudinal subdivision within the electromagnetic, fine hadronic and coarse hadronic sections is useful to help distinguish electrons and hadrons via their longitudinal shower profiles.

The η region $0.8 < |\eta| < 1.4$ in the DØ calorimeter contains a large amount of material in the walls of the cryostat because of the transition from the central to end regions. To measure the energy deposited in the uninstrumented walls, two scintillation counter arrays called intercryostat detectors (ICD) and separate single-cell structures called massless gaps were built. Each ICD consists of 384 scintillator tiles. Massless gap modules consist of two signal boards surrounded by three liquid argon gaps located inside the end cryostats. The size of readout cells of ICD and massless gaps is $\Delta\eta \times \Delta\phi = 0.1 \times 0.1$ exactly matching the liquid argon calorimeter cells.

2.2.4 Jet Identification

Jets appear as a localized cluster of energy deposited in the calorimeter and hence jet identification is completely dependent on the calorimeter. Based on the vertex found by Level 0, scalar E_T and missing E_T are computed from the vector sum of E_T of all calorimeter towers. The calorimeter hardware trigger (Level 1 Trigger) uses sums of the energy deposited in each trigger tower ($\Delta\eta \times \Delta\phi = 0.2 \times 0.2$) up to $|\eta| < 4.2$. These trigger tower are further divided longitudinally into electromagnetic trigger towers and hadronic trigger towers depending on the longitudinal location of the energy. Events are selected as jet candidates if the sum of the electromagnetic and hadronic trigger towers exceeds various trigger thresholds.

Events passing the hardware trigger are further processed via a software trigger filter (Level 2 Trigger). For jet triggers, a $R = 0.7$ cone is drawn after the sum of E_T within a precluster ($R = 0.3$) around the seed tower ($\Delta\eta \times \Delta\phi = 0.1 \times 0.1$) passes a threshold cut. Since the data acquisition system can not record all triggers, events are prescaled in different regions. The rejection factor (prescale) of triggers needed for the physics analysis is determined by the bandwidth of the data acquisition system. Finally events are selected by imposing thresholds in jet E_T and η used by various jet analysis in different kinematic regions. Details of data acquisition, jet algorithm and reconstruction will be discussed in the next section.

2.2.5 Missing Transverse Energy ($\not{E}_T$) Measurement

The hermetic nature and the uniformity of the DØ detector facilitate measuring the missing transverse energy of events. Since the initial transverse momentum of the proton-antiproton system is expected to be small and the detector covers almost the entire solid angle, the final transverse momentum is expected to be small as well. If large $\not{E}_T$ is present, this is taken as an indication of processes involving the production of weakly interacting particles such as neutrinos or suppersymmetric particles. In reality, however, there are other experimental sources of $\not{E}_T$ such as 1) detector noise, 2) energy resolution in the measurement of jets, photons, electrons and muons, and 3) dead regions or non-uniformity of response in the detector. It is important to measure this experimental contribution of $\not{E}_T$ to gauge the sensitivity of the detector to real $\not{E}_T$ sources. In jet analysis this information is used for removing bad events and extracting the detector response. The measurement of $\not{E}_T$ is done by summing all transverse energy of calorimeter cells and looking for an imbalance. If there are muons, their momenta is also added assuming that all the energy in a cell is deposited at the center of the cell.

Chapter 3

Data Acquisition and Reconstruction

The DØ data acquisition system is normally capable of recording about three interactions out of approximately 10^5 $p\bar{p}$ interactions per second occurring at the Tevatron. To select interesting physics events, the DØ experiment uses three main selection criteria: Level 0 trigger for inelastic collisions, Level 1 hardware triggers, and Level 2 software triggers. The DØ data acquisition and trigger system are described in detail in elsewhere [19]. The data of interest to this analysis are the events with at least two jets each with $\mathrm{E}_T \geq 20$ GeV. Since this analysis emphasizes events with two jets on opposite sides at large pseudorapidities, data were collected with a forward jet trigger with a constraint on jet η ($|\eta| > 1.6$) as well as a very low E_T threshold ($E_T > 12$ GeV). Special QCD No Tracking (QNT) runs were used to accumulate a large amount of jet data. Since the tracking information makes up the bulk of the data in an event and since it is not used in this analysis, eliminating the tracking in this subset of data allowed a large statistics sample to be collected in a much shorter time. QNT runs recorded QCD jet events at a rate of approximately 25 Hz. Collected data were reconstructed offline with a special project for QNT data. In this section, data acquisition and reconstruction related to this analysis and their efficiencies are described.

3.1 QCD No Tracking Data

QNT runs were specialized only for QCD jet triggers at a relatively low instantaneous luminosity ($\mathcal{L} < 5 \times 10^{30} cm^{-2} s^{-1}$). This analysis employed the JET_2 and JET_END_2 trigger at Level 1 (L1) which has corresponding JET_12_QNT and JET_END_12_QNT trigger filters at Level 2 (L2) from QNT special runs. Approximately 60 hours of QNT runs accumulated around 2.5×10^6 events for the two trigger filters during the 1994-1995 Tevatron Collider (1B) run. Events from these two runs account for approximately 60% of the total QNT data. The selection criteria for QNT data used for this analysis followings:

1) **LØ Trigger**: The Level 0 (LØ) trigger for QNT runs required an inelastic collision with a single interaction only. The inelastic collision rate was approximately 150 KHz at a luminosity of $\mathcal{L} = 5 \times 10^{30} cm^{-2} s^{-1}$ and the LØ trigger efficiency for triggering on inelastic collisions is greater than 99%. The LØ quality is the rms deviation of the time differences from the two LØ detectors. The single interaction portion of this trigger requires that the LØ quality is within a σ of the mean. The LØ trigger requirement is denoted as LØ(1).

2) **L1 Trigger**: The L1 trigger is a fast hardware trigger designed to select interesting events from among those passing the LØ trigger. The time available for the trigger decision is the 3.5 μs between bunch crossings. QNT data acquisition is based on the DØ calorimeter trigger which requires a certain transverse energy deposited in a fixed cluster of calorimeter shells. For this analysis, the JET_2 trigger required that one trigger tower (0.2×0.2 in η–ϕ) was above 2 GeV. The JET_END_2 trigger imposed an additional pseudorapidity constraint ($|\eta| > 2.0$) for the trigger tower. The E_T of trigger tower is calculated using the vertex from LØ. These L1 trigger

requirements are denoted as L1JT(1,2) and L1JT(1,2,Y2), respectively.

3) **L2 Trigger**: The L2 jet trigger is a software filter whose tools find jets and calculate their E_T within a fixed cone of radius $R = 0.7$ centered at all trigger tower coordinates in η–ϕ passing the L1 trigger thresholds. JET_12_QNT filter required that E_T of one jet be above 12 GeV while JET_END_12_QNT imposed an additional η restriction ($|\eta| > 1.6$) for the jet. For the run 1B, the L1 calorimeter trigger was implemented out to $|\eta| \leq 4.0$ which was significantly extended from $|\eta| \leq 3.2$ for the run 1A. This also limits L2 as a L1 seed tower is required to find a L2 jet. These L2 trigger requirements are denoted as L2JT(1,12) and L2JT(1,12,Y1.6), respectively. Triggers and filters used for the analysis are summarized in table 3.1.

Trigger Name	Filter Name	Level 0	Level 1	Level 2
JET_2	JET_12_QNT	LØ(1)	L1JT(1,2)	L2JT(1,12)
JET_2_END	JET_END_12_QNT	LØ(1)	L1JT(1,2,Y2)	L2JT(1,12,Y1.6)

Table 3.1: Level 1 trigger and Level 2 filter requirements placed on data sample.

3.1.1 Jet Trigger Efficiencies

Since the DØ jet trigger system uses rudimentary jet information from the calorimeter to reject uninteresting events in a very short time interval, there are some inefficiencies in selecting events above the stated jet E_T and η thresholds. Jet trigger inefficiencies are primarily due to the fixed size and position of the calorimeter towers, uninstrumented regions of the intercryostat detectors and massless gaps, and the reduced integration time of the calorimeter readout.

A set of special QCD Mark and Pass (QMP) runs was taken to determine the L1 and L2 trigger efficiencies. In the QMP run, an event is written to tape if it passes a L1 trigger. The relevant L2 filters are tested and the event is marked if it passes

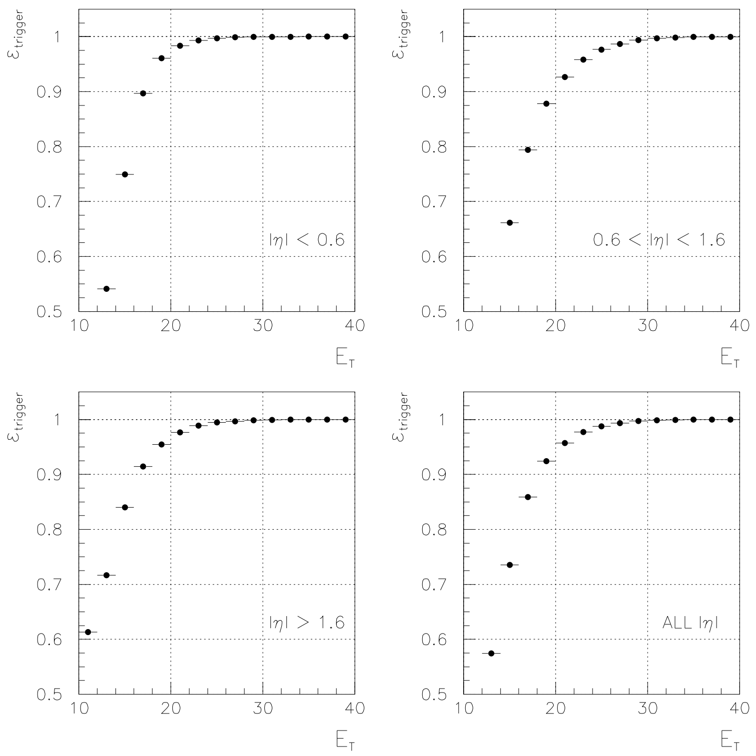

Figure 3.1: Average event efficiency for JET_12_QNT as a function of leading jet E_T in different η regions.

L2, but the event is kept whether or not it actually did pass the L2 filters. The L1 and L2 event efficiencies have been measured for 1B QNT jet triggers and filters [20]. For the JET_2 trigger, the L1 efficiency is calculated by using those events which pass a less restrictive trigger without requiring any condition for the L1 trigger tower (MIN_BIAS). The total event trigger efficiency to pass both L1 and L2 is simply the product of the two. Average event efficiencies for JET_12_QNT are shown in figure 3.1.

Since this study also uses the forward jet trigger (JET_END_12_QNT), it is necessary to determine where in η this trigger becomes fully efficient so that it can be

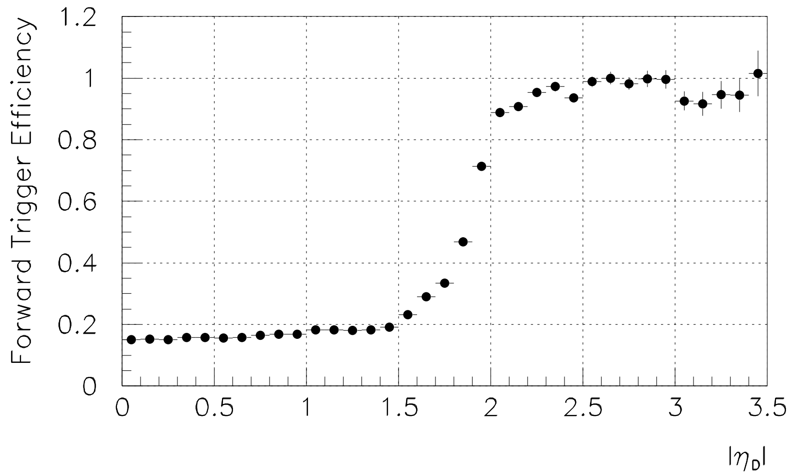

Figure 3.2: The relative JET_END_12_QNT to JET_12_QNT trigger efficiency as a function of detector η for jets with $E_T > 20$ GeV. The forward trigger efficiency is greater than 95% at $|\eta| > 2.25$.

combined with the inclusive η trigger without any bias. The relative forward trigger efficiency for $E_T^{jet} > 20$ GeV compared to the JET_12_QNT is estimated by dividing $dN/d\eta$ of JET_END_12_QNT by that of JET_12_QNT. The resulting efficiency which is shown in figure 3.2. To ensure the full relative trigger efficiency in η for JET_END_12_QNT, we require that at least one jet with $E_T > 20$ GeV must be above $|\eta| = 2.25$. Necessary corrections due to trigger inefficiencies for dijet events used for the analysis will be described in the systematic section 5.3.

3.2 Jet Reconstruction

The physical manifestation of colored partons as sprays of colorless hadrons are referred to as jets. At the DØ experiment, jets are identified as a localized cluster of energy deposits in the colorimeter and quantified by various jet algorithms. For this analysis, we use jets reconstructed offline using the standard Snowmass algorithm [3] with a cone of radius $R = 0.7$ in η–ϕ space. Specific parameters and procedures of the cone jet algorithm are included in specific reconstruction projects for the full data reconstruction at DØ. QNT data was reconstructed using DØ RECO V12.15, V12.20, and V12.21 with a "No Muon Hit" special project (RECO_FULL_NOMH) with the choice of parameters controlled by CAJETS_QNT.RCP. The reconstructed data summary files (DST) with different reconstruction versions were then refined and unified by the DØFIX project. In this section, we review the iterative cone algorithm used at DØ and reconstruction the efficiency.

3.2.1 The Iterative Cone Algorithm

Jet finding at DØ uses the E_T of the calorimeter towers which is determined from the energy vector of towers:

$$\vec{E}^{tower} = \sum_{i=cells} \hat{n}_i E_i, \tag{3.1}$$

$$E_T^{tower} = \sqrt{(E_x^{tower})^2 + (E_y^{tower})^2}, \tag{3.2}$$

where $\hat{n}_i$ is the unit vector pointing from the interaction point to the center of calorimeter cell i, and E_i is the magnitude of the energy deposited in cell i. The algorithm is then implemented as a series of iterative steps: preclustering, cone clustering, and jet splitting or merging.

Preclustering begins with an E_T ordered list of calorimeter towers ($\Delta\eta \times \Delta\phi = 0.1 \times 0.1$) which have an $E_T > 1$ GeV. The highest tower is taken as a precluster seed. Centered at the η, ϕ position of the seed tower, a precluster is formed by summing the E_T of all towers having $E_T > 1$ GeV within a cone of radius $R = 0.3$. The towers included in the precluster are then removed from the seed list and the remaining towers with the highest E_T is used as the next seed. This continues until no seed remains in the list.

The next step of reconstruction, jet clustering, begins with the ordered list of preclusters in descending E_T which are used as seeds for jet cones. Centered at the η–ϕ position of the highest E_T precluster, the E_T of all towers within a cone of radius $R = 0.7$ is summed and assigned to a jet. The E_T weighted centroid of the jet is calculated as followings:

$$
\begin{aligned}
E_T^{jet} &= \sum_i E_{Ti}, && (3.3)\\
\eta^{jet} &= \frac{\sum_i E_{Ti} \times \eta_i}{\sum_i E_{Ti}}, && (3.4)\\
\phi^{jet} &= \frac{\sum_i E_{Ti} \times \phi_i}{\sum_i E_{Ti}}, && (3.5)
\end{aligned}
$$

where i is the index for all towers in the jet. This process continues until the calculated centroid of the jet converges within a radius $R = 0.001$ of the previous centroid of the jet. The maximum number of iteration is set to 50 to avoid the possibility of a jet center oscillating between two centers. The resulting jet is stored if it passes the minimum E_T of jet to be reconstructed (8 GeV).

Since cone jets can overlap, it is necessary to consider merging or splitting of the jets. The first jet by definition can share no energy with a previously found jet. Beginning with the second, each new jet is checked to see whether it shares any towers with previously found jets. If one or more towers are shared, the jet is either merged or split with the overlapped jet using the fraction of shared E_T divided the lesser of the E_T of the two jets. If the fraction is greater than 0.5, two jets are merged into a single jet adding all the towers within them. Otherwise, two jets are split into separate jets by assigning each shared cell to the jet whose center is the closest to the cell. In either case the jet axis is recalculated one last time, including all the appropriate towers without any further iterations.

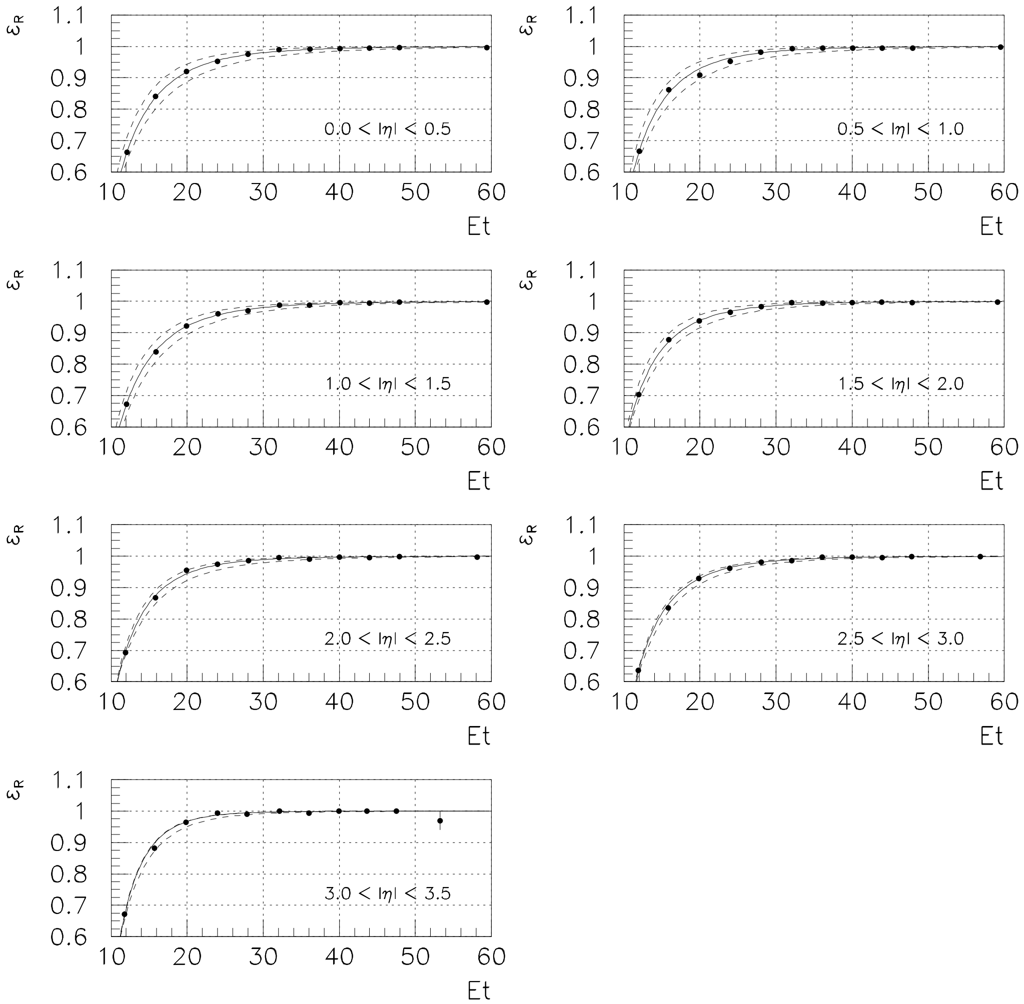

Figure 3.3: Jet reconstruction efficiencies as a function of particle jet E_T in different η regions. The functional form of the fit is $\epsilon_R(E_T) = 1 - C_0 e^{-(\frac{E_T}{C_1})^{C_2}}$. The center band shows the nominal efficiencies obtained with $\Delta R < 0.5$ while the upper (lower) band is obtained with $\Delta R < 0.7$ ($\Delta R < 0.3$), where ΔR is the distance from the center of the particle jet.

3.2.2 Jet Reconstruction Efficiencies

An ideal detector and reconstruction jet algorithm may find any initial spray of particles as the signature of a final state parton shower deposited in the calorimeter. Since the DØ detector is hermetic, there is no significant geometrical inefficiencies in jet finding for jets with $\eta \leq 4.0$. However, there are certain inefficiencies in the jet reconstruction procedure due to parameters used such as the radius of the cone, the minimum seed threshold of calorimeter towers, and the minimum E_T for jet reconstruction as well as the intrinsic jet energy resolution of the detector. The jet reconstruction efficiency is expected to be the worse at the E_T threshold of the jets to be reconstructed, but to approach to 100% as the E_T of the jet moves away from this threshold.

A simple estimation of reconstruction efficiency based on a Monte Carlo study has been done by matching positions between the reconstructed calorimeter jet and the particle jet for HERWIG events that were processed through the detector simulation (DØGEANT) and the reconstruction. The efficiency is calculated by testing whether a calorimeter jet is found within a certain geometrical matching criteria around the center of a particle jet. This study shows that this algorithm is more than 90% efficient for reconstructing jets with $\mathrm{E}_T > 20$ GeV in all η regions considered. The jet reconstruction efficiencies from particle jets as a function of particle jet E_T and η are shown in figure 3.3. This study also shows no significant loss of efficiency in the forward region of the detector.

Chapter 4

Calorimeter Jets

Reconstructed jets as localized energy clusters in the calorimeter consist of many different type particles as a result of the fragmentation of partons to hadrons. An ideal detector and jet reconstruction algorithms will measure the same kinematical variables as for the underlying parton jet above a certain E_T threshold. In reality, measured kinematical jet variables in the detector differ from those of jets associated with the remnant of partons within a cone in the hard scattering process. At DØ, the true jet energy is defined as the sum of all the final state particle energies in a fixed cone of size R that matches a jet measured in the calorimeter with the same algorithm. Therefore it is necessary to correct the measured energy of jets based on detector information as well as background from specific physics processes and experimental running conditions. After the jet energies are properly corrected, the average of the corrected jet energy will be the same as the true jet energy with certain intrinsic experimental resolutions due to detector effects and the jet algorithm. In this section, we describe jet energy corrections, jet energy and position resolutions, and the removal of bad events and jets.

4.1 Jet Energy Corrections

The energy of a jet is measured in central (CC) and forward (EC) liquid argon-uranium calorimeters using a calibration obtained from a test beam consisting of single pions of known energy [21]. The uncorrected jet E_T refers to the measured energy based on the calibration during the jet reconstruction. In the DØ calorimeter there is a significant non-linearity in the calorimeter's energy response to pions of incident energies lower than approximately 10 GeV. Since many particles even in a high energy jet are of low energy, it is necessary to correct the reconstructed jet energy to recover the energy of all particles contained within the jet cone. The measured jet energies are also affected by uranium noise from the decay of nuclei in the calorimeters, energy from the previous interaction (pileup), and energy deposited from beam remnants and spectator interactions (underlying event). Furthermore, there is an additional jet algorithm dependent correction due to hadron showering which adjusts for the detector-based showering loss for the fixed cone jets.

The total jet energy correction can be expressed in the following form:

$$E^{jet}_{particle} = \frac{E_{measured} - O}{(1-S)R_{had}}, \tag{4.1}$$

where O is the total offset due to uranium noise, pileup, and the underlying event, and S is the calorimeter showering loss, and R_{had} is the calorimeter hadronic response. The overall jet energy scale correction is described in detail elsewhere [22, 23]. Here we just briefly review the method to determine the hadronic response which is the dominant factor in jet energy corrections.

The hadronic response of the calorimeter is determined by the so-called 'MPF' (Missing E_T Projection Fraction) method originally developed by the CDF collaboration [24]. In general the MPF method uses the conservation of transverse energy in photon candidate events with at least one 0.7 cone jet. Since the measured energy of a photon is well known, any imbalance in the E_T in a photon-jet event can be interpreted as an error in the energy measurement of the jet. To minimize the

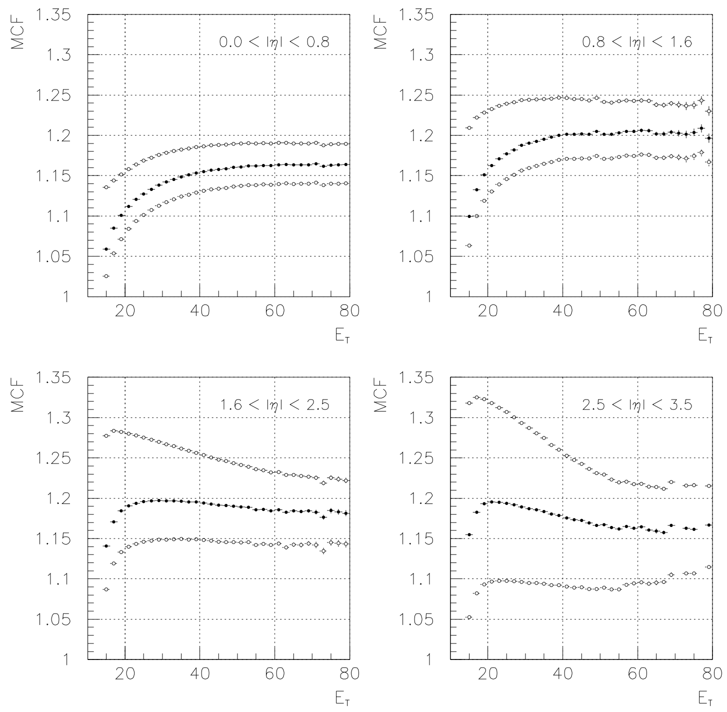

Figure 4.1: Mean correction factor of jet energy scale correction for samples used for this analysis as a function of jet E_T in different η regions. The central points represent the nominal correction factor while upper and lower points represent uncertainties of the mean correction factor.

imbalance contribution due to particles radiated outside of the jet cone, the ratio of the component of the $\not{E}_T$ projected in the direction of the photon ($\hat{n}^\gamma$) over the E_T of the photon (E_T^γ) is used. The absolute hadronic response relative to the photon is given by

$$R(E^{'}) = 1 + \frac{\vec{\not{E}}_T \cdot \hat{n}^\gamma}{E_T^\gamma}, \tag{4.2}$$

where $E^{'} = E_T^\gamma \cdot \cosh(\eta_{jet})$. The reason for using $E^{'}$ instead of the jet energy is because the photon E_T and the jet pseudorapidity are well resolved. The quantity

$R(E^{'})$ measures the response of the calorimeter for the hadronic recoil independent of jet algorithm chosen. The hadron response as a function jet energy are then obtained by a mapping between $E^{'}$ and jet energy for each jet algorithm separately.

The response at low to moderate $E^{'}$ (10 GeV $< E^{'} <$ 150 GeV) is determined from low E_T photons and CC jets ($|\eta| < 0.7$) while EC ($1.8 < |\eta| < 2.5$) jets are used for high values of $E^{'}$ (100 GeV $< E^{'} <$ 400 GeV) [23]. The forward measurement is normalized to the central measurement by the value obtained by the ratio of EC response to CC response (the cryostat factor). The overall jet energy scale correction used on samples used for this analysis is shown in figure 4.1.

4.2 Jet Energy Resolution

The DØ calorimeter has an intrinsic limit on the jet energy resolution since it is a sampling calorimeter. Jet energy resolution is also inherently limited from other characteristics of the detector such as the non-linear response of the calorimeter for low energy hadronic particles, the response difference between electromagnetic particles and hadronic particles, and detector noise. In general low energy jets have poor energy resolution because they are more vulnerable to all these effects. On the other hand, the E_T spectrum of jets is a steeply falling function so that jets are more likely to fluctuate to higher E_T regions. As a result, any observed physical variable will be affected by the jet energy resolution if it depends on either the jet energy itself or certain event selection cuts. Hence it is necessary to estimate the jet energy resolution to study its effect on measured variables explicitly or implicitly. The jet E_T resolution at a fixed η bin will be equivalently used for the jet energy resolution.

The jet energy resolution as function of jet E_T and η has been measured from collider dijet events using the transverse momentum balance between two jets [25]. The balance is measured by using the jet asymmetry defined as

$$A = \frac{E_{T1} - E_{T2}}{E_{T1} + E_{T2}}, \tag{4.3}$$

η Region	N	S	C
$\|\eta\| < 0.5$	5.97±0.12	0.80±0.02	0.00±0.01
$0.5 < \|\eta\| < 1.0$	6.61±0.19	0.68±0.06	0.00±0.01
$1.0 < \|\eta\| < 1.5$	1.83±2.34	1.14±0.13	0.05±0.01
$1.5 < \|\eta\| < 2.0$	7.17±0.35	0.56±0.12	0.09±0.04
$2.0 < \|\eta\| < 3.0$	6.09±0.23	0.71±0.06	0.00±0.07

Table 4.1: Parameters for jet E_T resolution as a function $\frac{\sigma_{E_T}}{E_T}$ in different regions of η.

and the jet E_T resolution is obtained as follows:

$$\frac{\sigma_{E_T}}{E_T} = \sqrt{2}\sigma_A, \tag{4.4}$$

where it is assummed that $E_T = E_{Ti}$ and $\sigma_{E_T} = \sigma_{E_{Ti}}$ with $i = 1, 2$ for deriving σ_A. The jet E_T resolution is then parameterized as a function of jet E_T:

$$\frac{\sigma_{E_T}}{E_T} = \sqrt{\frac{N^2}{E_T^2} + \frac{S^2}{E_T} + C^2}, \tag{4.5}$$

where N describes the contribution to the detector noise and underlying event, S to the shower fluctuation in the sampling, and C to calibration errors of the detector. The resulting parameterization is summarized in table 4.1.

In general the dijet balance method is expected to work very well for high E_T jets because the methodology is less sensitive to unreconstructed soft radiation in the event as well as causes of energy resolution smearing as mentioned earlier. However, the method is questionable for estimations of the jet E_T resolution at $E_T < 20$ GeV and at the very forward region of the detector ($\eta > 2$) where the jet characteristics are more uncertain. Since this analysis employs jets $E_T \sim 20$ GeV and jets in a very forward region, we have estimated jet E_T resolution for this analysis based on a Monte Carlo method that matches particle jets to corresponding calorimeter jets

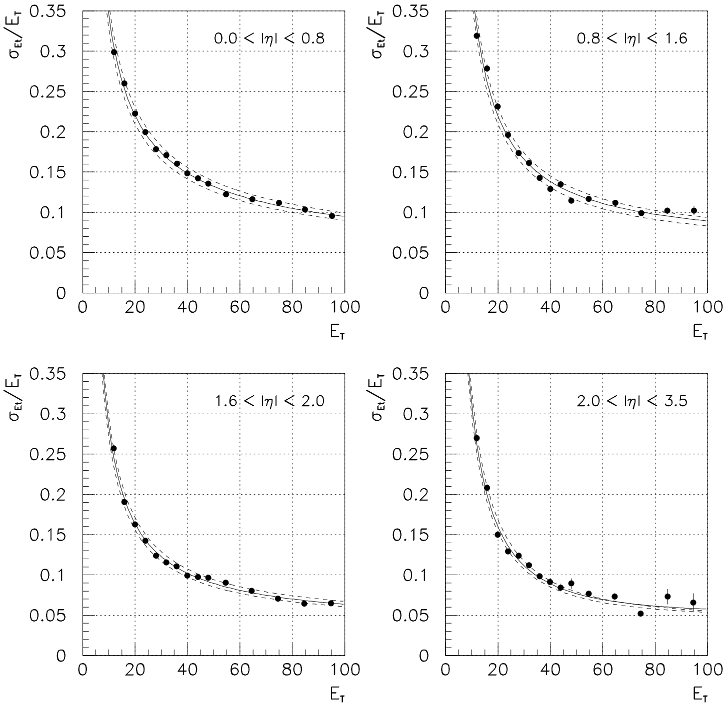

Figure 4.2: Jet E_T resolution as a function of particle jet E_T in different η regions. The dotted band represents the range of uncertainties due to jet energy scale corrections.

after the detector simulation, noise overlapping, and reconstruction and energy scale correction. HERWIG V5.8 samples generated with underlying events are overlapped with noise events (ZERO_BIAS) taken at $\mathcal{L} = 3.29 \times 10^{30} cm^2 s^{-1}$. A reconstructed and energy corrected jet is then matched to the corresponding particle jet within $\Delta R < 0.3$ around the center of the particle jet. The standard deviation of a gaussian fit to the distribution of $E_T^{calorimeter}/E_T^{particle}$ is attributed to estimated particle jet E_T resolution as a function of the particle jet E_T which is shown in figure 4.2. The particle jet E_T resolution will only be used to smear particle jet Monte Carlo samples and to estimate jet energy resolution effects on this analysis.

4.3 Jet Position Resolution

The jet position in η–ϕ space has an intrinsic experimental resolution due to both detector effects and the jet algorithm used. The E_T weighted position of the jet in the calorimeter (Eq 3.4 and 3.5) is different from that of the corresponding partons due to the non-linear hadronic response and the fixed size of calorimeter cells. The η and ϕ position resolution of the jet are separately measured by comparing parton jets and reconstructed calorimeter jets with HERWIG Monte Carlo samples [26]. The variance of η and ϕ distributions as a function of jet energy and detector η was determined by measuring the variance of the distribution of the difference between the center of parton jet and that of the reconstructed jet. The resolution $\sigma_x(E,x)$ for $x = \eta, \phi$ is then parameterized as a function of parton jet energy in different pseudorapidity regions as follows:

$$\sigma_x(E,x) = A_x + \frac{B_x}{E} + \frac{C_x}{E^2}. \tag{4.6}$$

The estimated jet position resolutions are shown in figure 4.3 and figure 4.4 and the resulting parameterization is summarized in table 4.2.

η	A_η	B_η	C_η	A_ϕ	B_ϕ	C_ϕ
0.0-0.5	0.006663	0.7727	2.130	0.007554	0.5897	3.452
0.5-1.0	0.005418	1.164	1.230	0.007105	0.8484	5.042
1.0-1.5	0.005667	1.826	-5.847	0.005567	1.836	-10.80
1.5-2.0	0.003866	2.693	-13.84	0.006334	2.296	-15.85
2.0-2.5	0.0004306	5.578	-116.2	0.003316	4.787	-101.4
2.5-3.0	0.004273	8.637	-328.4	-0.001437	8.534	-346.7
3.0-3.5	-0.01897	19.64	-1241.	-0.01897	26.59	-2301.

Table 4.2: Parameterization of the jet η and ϕ resolution.

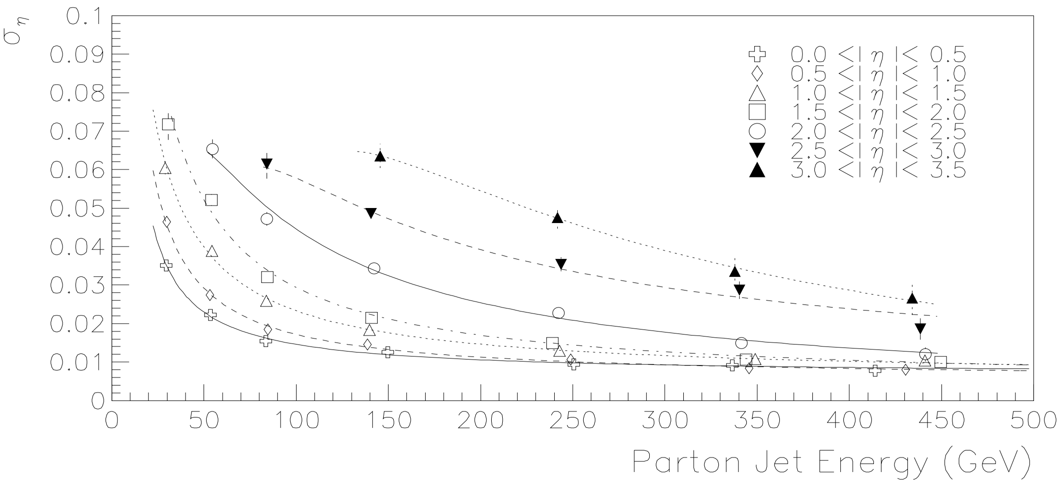

Figure 4.3: The η resolution from a HERWIG Monte Carlo simulation.

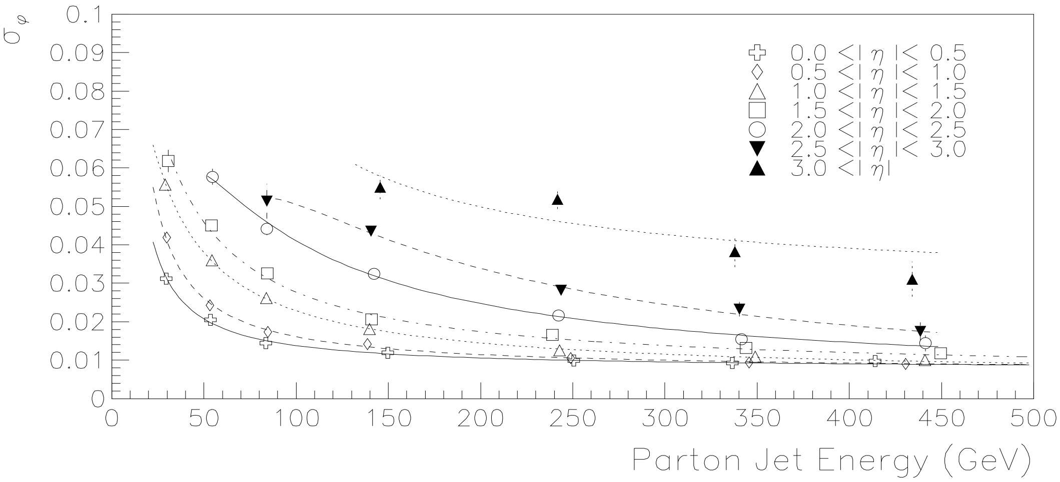

Figure 4.4: The ϕ resolution from a HERWIG Monte Carlo simulation.

4.4 Jet Quality Cuts and $\not{E}_T$ Cut

Reconstructed jets do not always originate from particles emanating from inelastic $p\bar{p}$ collisions. We define spurious jets as any reconstructed jet object which is not associated with specific physics processes from the $p\bar{p}$ collisions. The most common causes of spurious jets are noisy channels or fluctuations in a calorimeter channel readout, a change in a channel pedestal or a hardware problem, proton losses from the main ring of the Tevatron, cosmic ray bremstrahlung, and beam-gas interactions. Spurious jets for RUN 1B data were removed using the standard QCD good jet cuts [27].

The standard QCD good jet cuts use the electromagnetic energy fraction of the jet (EMFR), the ratio of the energy of the second most energetic jet cell to the most energetic cell in the jet (HCFR), and the coarse hadronic energy fraction (CHFR). A EMFR cut (EMFR < 0.95) removes spurious jets which are probably reconstructed from noisy cells located in the electromagnetic layer of the calorimeter or energetic electrons and photons. A HCFR cut (HCFR > 0.05) is designed to remove jets reconstructed from electronic noise. A CHFR cut (CHFR < 0.40) is designed to reject jets reconstructed by energy deposits from the main ring of the Tevatron. These cuts are greater than 98% efficient for all E_T and η regions of interest for this analysis. All three cuts will be applied over all η. The global efficiency for all three cuts is shown in figure 4.5.

Even though the standard good jet cuts are very efficient for removing spurious jets from events, some noise still survives. To remove the remaining localized noise or cosmic rays without degrading the good jet cut efficiencies, a $\not{E}_T$ cut is introduced to reject the events having a large $\not{E}_T$ compared to the highest E_T jet (leading jet) in the event. For RUN 1B QCD jet triggers, a $\not{E}_T$ fraction cut, $E_T^{leadingjet}/\not{E}_T < 1.4$, is applied on an event by event basis. The $\not{E}_T$ cut efficiencies for QNT data are shown in figure 4.6.

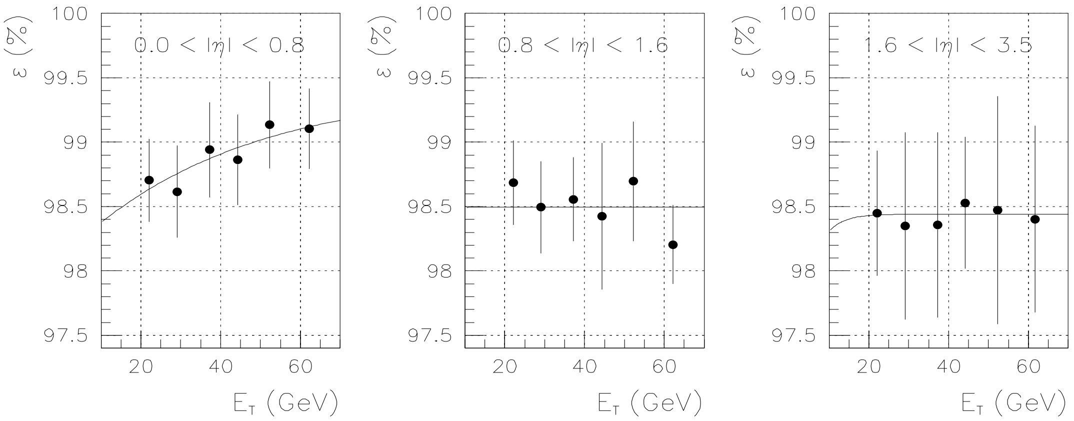

Figure 4.5: The efficiency of good jet cuts as a function of jet E_T. The functional form of the fit in each η bin is $a \times \tanh[b \times (E_T + c)]$.

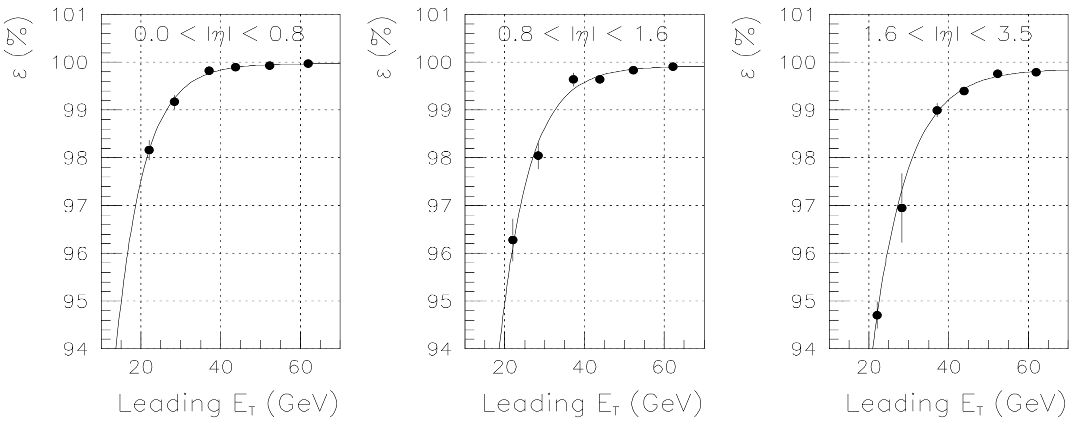

Figure 4.6: $\not\!\!E_T$ efficiency as a function of leading jet E_T. The functional form of the fit in each η bin is $a \times \tanh[b \times (E_T + c)]$.

Chapter 5

Azimuthal Decorrelation

Nature sometimes reveals her secrets of beauty through a series of proper selection procedures. Measuring the azimuthal decorrelation of jets widely separately in rapidity is essentially a statistical experiment to probe higher order QCD effects or a possible signature of BFKL dynamics at the Tevatron. Approximately two and one-half million events taken during Run 1B and 1C QNT special runs allow us to measure the azimuthal decorrelation variable ($<\cos(\pi - \Delta\phi)>$) with $< 5\%$ statistical errors over the six units of rapidity studied. Since the azimuthal decorrelation depends on tagging two jets at extremes of rapidity correctly, a series of event and jet selection cuts are imposed to remove most of the contamination in the data sample. Selection biases and intrinsic experimental uncertainties will be taken into account either with a correction or a systematic error. In this chapter, we describe offline selection cuts to measure the azimuthal decorrelation as a function of rapidity interval and the related experimental systematics. Systematic studies are primarily focused on $<\cos(\pi - \Delta\phi)>$. Along with experimental results, we also present predictions based on parton shower Monte Carlos to understand the physics related to this analysis as well as to compare to the data.

5.1 Event Selection

To study the azimuthal angle decorrelation, we use two single jet filters (JET_12_QNT and JET_END_12_QNT), and select inclusive dijet events that have at least two jets with $E_T > 20$ GeV within $|\eta| < 3.5$. The fixed cone jet algorithm with $R = 0.7$ is used with the Snowmass angle definition for η and ϕ position of the jet [3]. A series of cuts are imposed to remove events contaminated by cosmic rays, instrumental noise, and multiple interactions as well as events with a vertex far from the nominal center of the detector. Jet quality cuts are applied on a jet-by-jet basis in each event to remove spurious jets. Jets are ordered by their pseudorapidities, the tagging jets being those at the extremes of psuedorapidity after a boost cut has been imposed ($|\bar{\eta}| < 0.5$). To avoid any ambiguities of the jet reconstruction algorithm, we require that both of the tagging jets are not complicated jets, neither merged nor split. This section describes offline selection requirements placed on jets and events to ensure event quality of the data sample. Any inefficiencies, selection biases and possible remaining contamination will be taken into account in the section on experimental systematics. Jet energy scale corrections have been applied before any event section.

5.1.1 Vertex Cut

Since the QNT data were taken without tracking information, the FAST z-vertex was used to impose a vertex cut ($|Z_{vtx}| < 100$ cm) applied during data taking. A single vertex requirement was also applied for all QNT triggers. The interaction vertex for samples used for this analysis has a Gaussian distribution centered at $< Z_{vtx} >= (0.80 \pm 0.02)$ cm with $\sigma = (25.48 \pm 0.02)$ cm. Since a large vertex offset may cause detector effects due to the fixed positions of the calorimeter towers, the event vertex is required to lie within:

$$|Z_{vtx}| < 50 \text{ cm} \tag{5.1}$$

of the nominal vertex. The efficiency of this vertex cut is 93.8%.

5.1.2 Single Interaction Cut

Since the QNT data were taken at low luminosity ($\mathcal{L} < 5.0 \times 10^{30} cm^{-2} sec^{-1}$) and with a single interaction requirement at LØ using the LØ quality information, most events are expected to be single interaction events. The multiple interaction tool (MITOOL) [28] is a more accurate indicator of multiple interactions, but it is not fully available for QNT data because of the lack of tracking information. For all QNT data, only those flag values indicating that the event is most likely a single interaction (MITOOL=1) or most likely a multiple interaction (MITOOL=4) are available. Events with MITOOL=4 are strongly correlated with the total energy (E_TOT) deposited in the calorimeter since the multiple interaction tool uses the total energy information as well as tracking information. Throughout this analysis, only single interaction events (MITOOL=1) with a reasonable total energy deposition in the entire calorimeter (E_TOT < 1800 GeV) are considered. Approximately 5% of the events are rejected by these cuts. Since jets from two different events are kinematically independent of each other, this measurement is very sensitive to multiple interactions. Any remaining contamination with multiple interactions in single interaction events has been studied using the distribution of E_TOT, which will be discussed in the section on experimental systematics.

5.1.3 Missing E_T ($\not{E}_T$) Cut

Cosmic rays produce spurious jets with unreasonably high (non-physical) $\not{E}_T$ in the calorimeter. To remove this background, the $\not{E}_T$ of the event is compared with the E_T of the leading jet ($E_T^{leading}$) and events are selected with:

$$METFR = \frac{E_T^{leading}}{\not{E}_T} > 1.4. \tag{5.2}$$

Cosmic ray events with high $\not{E}_T$ are expected to produce a peak at the lower end of the $METFR$ distribution. The $METFR$ distribution for the sample used is shown

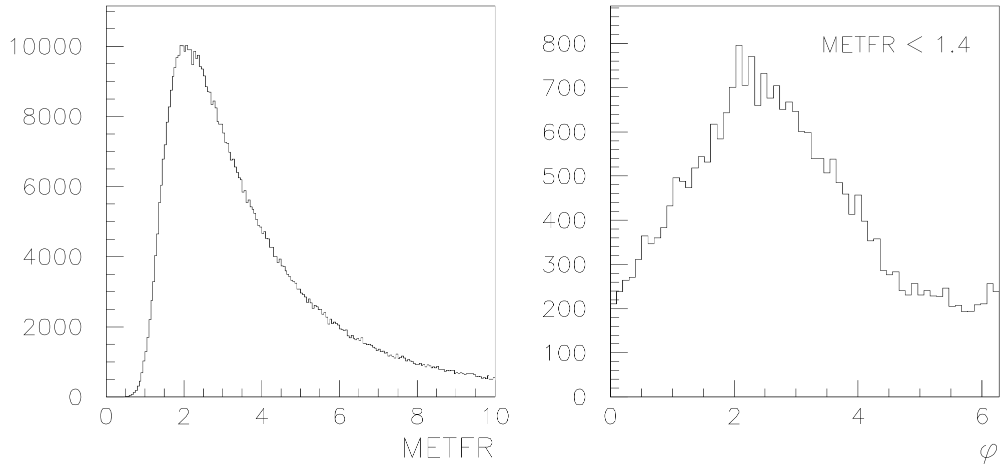

Figure 5.1: The METFR distribution for all events and the ϕ of the leading E_T jet only for events with $METFR < 1.4$. A trigger cut ($E_T^{leading} > 20$ GeV) and jet quality cuts have been imposed after the vertex and the single interaction cut.

in figure 5.1. In the plot, the vertex cut, the single interaction cut and a cut on the leading E_T jet ($E_T^{leading} > 20$ GeV) have been applied beforehand. The distribution is inclusive without applying any η or other $E_T^{leading}$ cuts. Unlike high E_T jet triggers, the noise peak below $METFR < 1.4$ is not clearly distinguishable in the plot. However this cut will be imposed to remove any possible contamination in the sample used, the presence of which may be indicated in the non-flat ϕ distribution of the leading E_T jet for events with $METFR < 1.4$. The $METFR$ distribution for low E_T triggers is shifted lower (~ 2) in comparison to higher E_T triggers (~ 4) resulting in an overlap of the distribution for cosmic ray events with that for events from real $p\bar{p}$ interactions. The overall efficiency of this cut after the previous cuts is 91.6%.

5.1.4 Jet E_T and η Cut

To ensure full reconstruction and trigger efficiency, additional transverse energy and pseudorapidity cuts are applied to the jets after each has been corrected for the calorimeter response. Since there is a significant loss of reconstruction efficiency below 20 GeV in the forward region as well as in the central region, only jets above this E_T are considered. In addition, since the calorimeter coverage extends only to $|\eta| = 4.2$, we require that all jet centers satisfy $|\eta| < 3.5$ allowing the entire cone radius of 0.7 to be contained in the calorimeter. Effects due to any residual inefficiency will be considered in the section on experimental systematics.

5.1.5 Jet Quality Cuts

Spurious jets were removed using the standard jet quality cuts that have been described in section 4.4,

$$\begin{aligned} EMFR &< 0.90, && (5.3) \\ CHFR &< 0.40, && (5.4) \\ HCFR &< 20.0. && (5.5) \end{aligned}$$

Any jet failing these cuts is removed from the event, but the event will be kept if the remaining jets pass subsequent selection cuts. As shown in figure 4.5, the overall efficiency of jet quality cuts is approximately 98%. Although jet quality cuts remove most of the spurious jets, they also introduce an additional bias in the final event sample due to removal of real jets. To reduce this effect, we also reject events having more than two jets failing the quality cuts. This cut is very effective in removing the bias introduced by removing spurious jets, yet the rejection rate is very small since it affects only events with four or more jets.

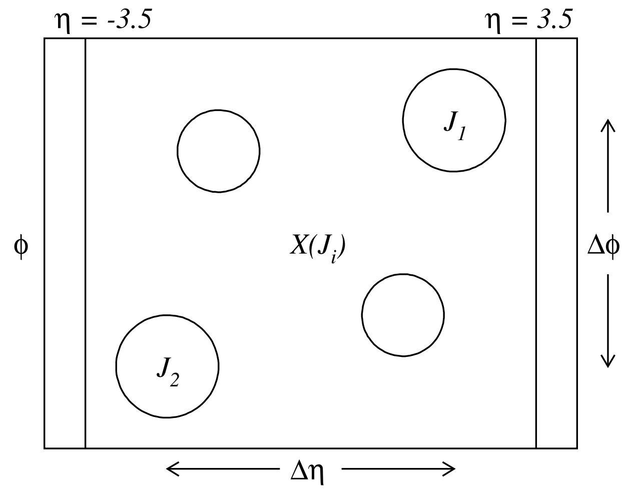

Figure 5.2: A typical event topology in $\eta - \phi$ space. J_1 and J_2 represent the two tagging jets while $X(J_i)$ represents all the hadron activity in the rapidity interval between J_1 and J_2.

5.1.6 Inclusive Dijet Events Ordered in Rapidity

Inclusive dijet events having at least two jets passing all previous cuts have been selected and their jets are ordered in rapidity:

$$\eta_1 > ... > \eta_2. \tag{5.6}$$

The two tagging jets are selected at the extremes of rapidity: the most forward jet is denoted as $J_1(E_{T1}, \eta_1, \phi_1)$ and the most backward as $J_2(E_{T2}, \eta_2, \phi_2)$. The physical quantities of interest, the rapidity interval $\Delta\eta$, the event boost $\bar{\eta}$, and the azimuthal angle difference $\Delta\phi$, of the tagging jets are defined as follows:

$$\Delta\eta = \eta_1 - \eta_2, \tag{5.7}$$

$$\Delta\phi = sgn(\phi_1 - \phi_2) \times (\phi_1 - \phi_2), \tag{5.8}$$

$$\bar{\eta} = \frac{1}{2}(\eta_1 + \eta_2). \tag{5.9}$$

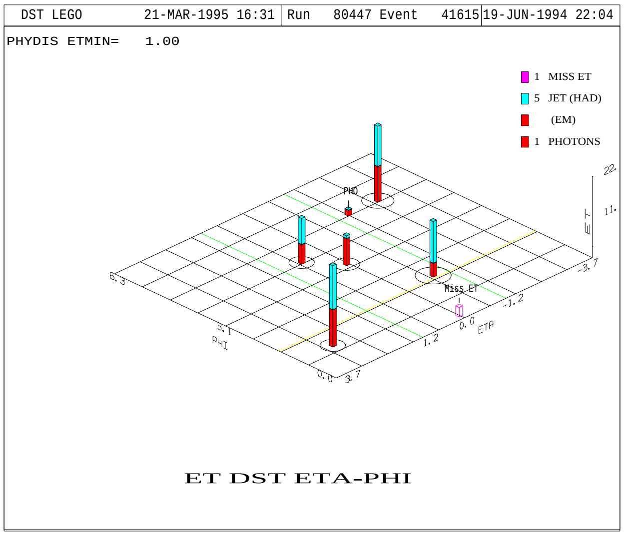

Figure 5.3: An example of multi-jet event with $\Delta\eta = 5$.

The definition of the boost is different from the usual boost definition ($\eta^* = \eta_1 + \eta_2$) by 2. A typical event configuration is shown in figure 5.2. For the forward trigger, at least one of the two tagging jets is required to be forward ($|\eta| > 2.25$) to ensure full trigger efficiency in η, and events from this trigger are used only for $\Delta\eta \geq 4.5$ to ensure full acceptance.

5.1.7 Rapidity Boost ($\bar{\eta}$) Cut

We require the rapidity boost of two tagging jets to be:

$$|\bar{\eta}| = \frac{1}{2}|\eta_1 + \eta_2| < 0.5. \tag{5.10}$$

This cut originally was introduced to avoid any possible small-x evolution problems in the parton distribution function and for theoretical convenience. Since the smallest x in this analysis is $\approx 2 \times 10^{-3}$, it is not really necessary to impose this cut. Nonetheless, it turns out that the boost cut is very efficient in reducing the reconstruction inefficiencies and the trigger bias of the forward trigger. Furthermore, the azimuthal

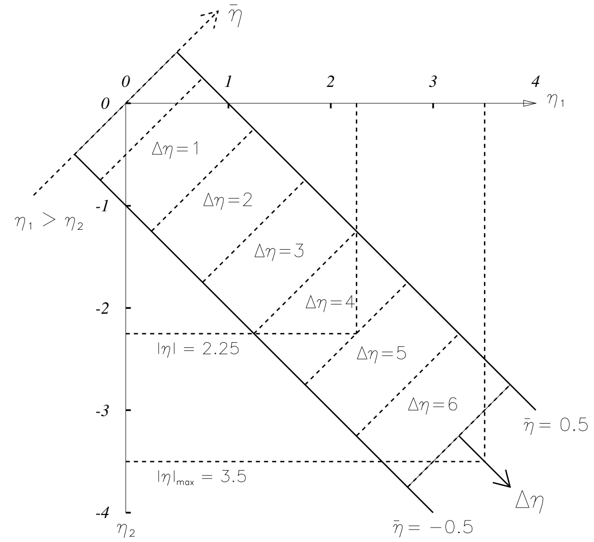

Figure 5.4: Tagging jets acceptance in $\eta_1 - \eta_2$ space.

decorrelation systematically varies in different $\bar{\eta}$ regions especially in the small $\Delta\eta$ bins, which are mainly attributed to the fractional difference of merged and split jets as a function of η. For central rapidities, jets are more likely to be merged or split than in the forward regions. Details of the necessity of and dependence on the $\bar{\eta}$ cut will be discussed in the systematic section. An example of an event passing all selection cuts is shown in figure 5.3.

5.1.8 Binned in Each $\Delta\eta$

Events passing all analysis cuts have been divided into unit $\Delta\eta$ bins, except for the lowest bin ($0.0 < \Delta\eta < 0.5$) which is half as wide. The n^{th} unit $\Delta\eta$ bin ranges from $n - 0.5$ to $n + 0.5$ up to $n = 6$. The final event selection region in $\eta_1 - \eta_2$ space is shown in figure 5.4. E_T, η, and ϕ distributions of the two tagging jets are shown in figure 5.5. Events from the forward trigger are used only in $\Delta\eta = 5$ and 6. All distributions will be plotted at the average value of $\Delta\eta$ for each bin to properly take into account the steeply falling $\Delta\eta$ distribution as shown in figure 5.6.

5.2 Azimuthal Decorrelation

In leading order QCD, the two outward going jets must be completely correlated since they are back-to-back in azimuth and balanced in transverse momentum. In higher order processes, the correlation of the two jets is eventually weakened due to additional radiation. To look for evidence of additional radiation as a function of the rapidity interval, the number of jets has been studied as an indirect signature of the azimuthal decorrelation. Measuring the triple differential cross section $d^3\sigma/d\Delta\eta d\bar{\eta} d\Delta\phi$ gives the qualitative characteristics of the decorrelation. In each $\Delta\eta$ bin, we measure the normalized $\Delta\phi$ distribution to see this qualitative decorrelation. In addition, we define a correlation variable, $< \cos(\pi - \Delta\phi) >$ to study this effect quantitatively. In this chapter, we describe these measurements as a function of $\Delta\eta$ (up to $\Delta\eta = 6$).

5.2.1 Jet Multiplicity

The degree of decorrelation of the two tagging jets is strongly related to the amount of additional radiation which may manifest itself as additional jet activity (M $\equiv$ jet multiplicity). We plot $< M - 2 >$ for jets with $E_T > 20$ GeV as a function of $\Delta\eta$ in figure 5.7. As $\Delta\eta$ increases, the average multiplicity increases, which indicates more hadron activity at large rapidity intervals. From the plot, the multiplicity increases linearly and has a relationship $< M-2 > \sim 0.08 \times \Delta\eta$. However, this does not directly quantify the decorrelation since jets below 20 GeV or any other soft radiation are not considered. Furthermore, the increase of multiplicity may also be due to the larger kinematical space allowed for radiation between the two tagging jets as their rapidity interval increases.

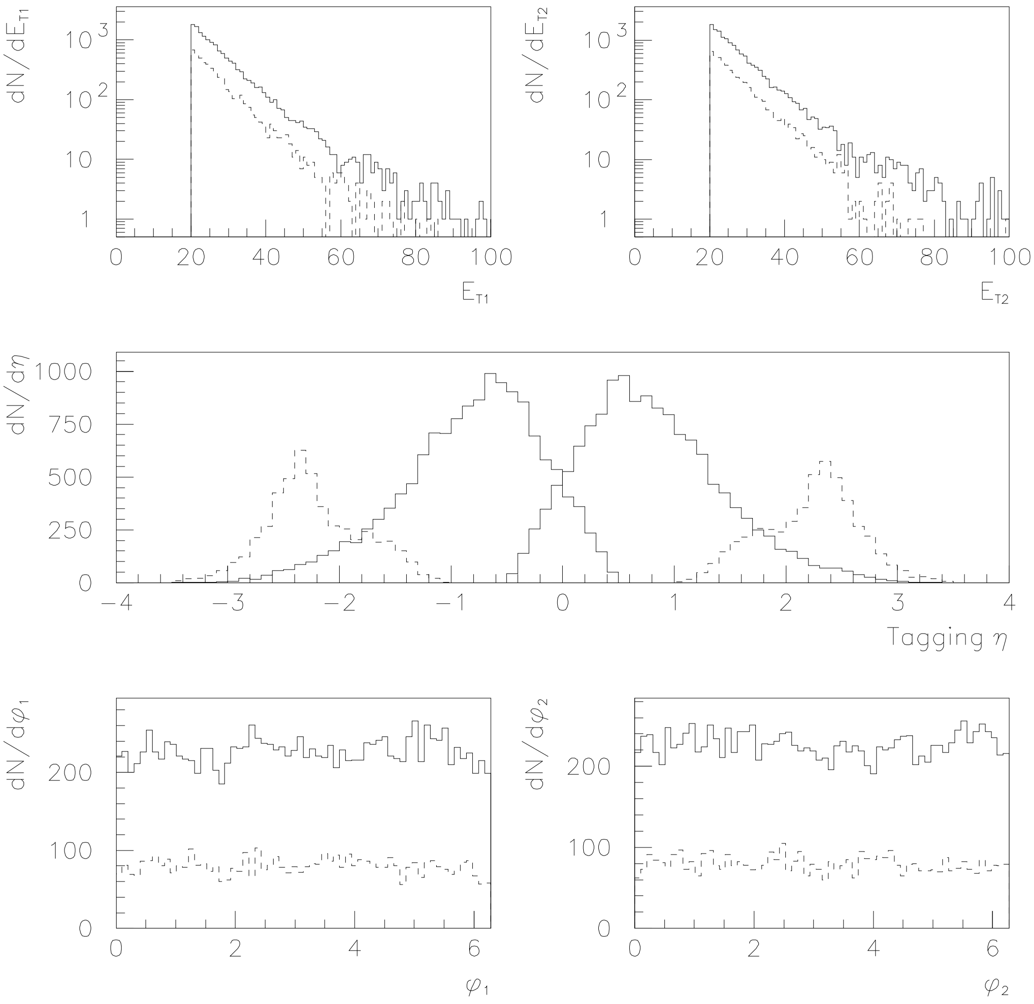

Figure 5.5: The E_T, η, and ϕ distributions of the two tagging jets. Solid histograms are for JET_12_QNT and dotted are for JET_END_12_QNT.

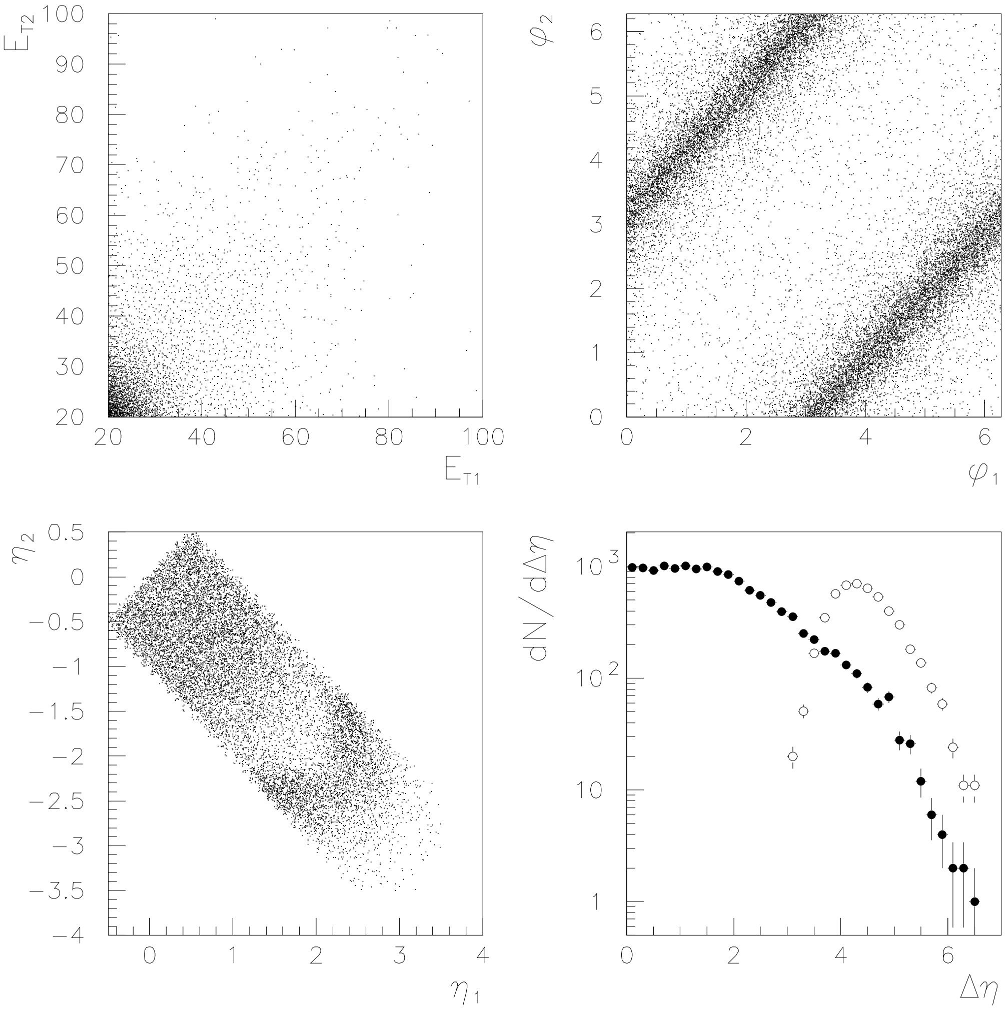

Figure 5.6: The event distributions in $E_{T1} - E_{T2}$, $\eta_1 - \eta_2$, and $\phi_1 - \phi_2$ space, and the $\Delta\eta$ distribution (closed circle marks are for JET_12_QNT and open for JET_END_12_QNT).

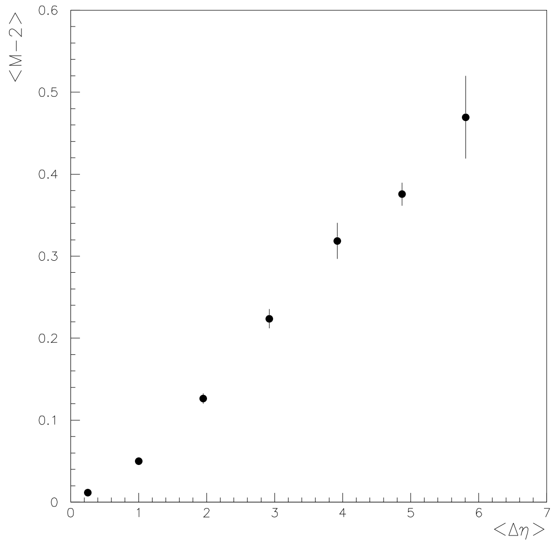

Figure 5.7: Jet ($E_T > 20$ GeV) multiplicity for $\Delta\eta$. Errors are statistical only.

5.2.2 $\Delta\phi$ Distribution

The widening of the $\Delta\phi$ distribution as $\Delta\eta$ increases is a qualitative feature of the azimuthal decorrelation. The normalized $\Delta\phi$ distribution, $1/NdN/d\Delta\phi$, with $\Delta\eta$ is equivalent to the two jet production rate $d\sigma/d\Delta\eta d\bar{\eta}\Delta\phi$ normalized to the uncorrelated one $d\sigma/d\Delta\eta d\bar{\eta}$. As the rapidity interval $\Delta\eta$ between the tagging jets is increased, more and more partons are produced which decorrelate the tagging jets in $\Delta\phi$. The azimuthal angular separation, $|1 - \Delta\phi/\pi|$, is plotted with unit bins centered at $\Delta\eta$ $= 1$ and 5 in figure 5.8. Using the fact that the $\Delta\phi$ distribution is symmetric, we fold the $1 - \Delta\phi/\pi$ about 0 by plotting its absolute value. Since each distribution is normalized to unity, the decorrelation between the two most widely separated jets can be seen in either the relative decline near $|1 - \Delta\phi/\pi| = 0$ or the relative increase near $|1 - \Delta\phi/\pi| = 1$ as $\Delta\eta$ increases.

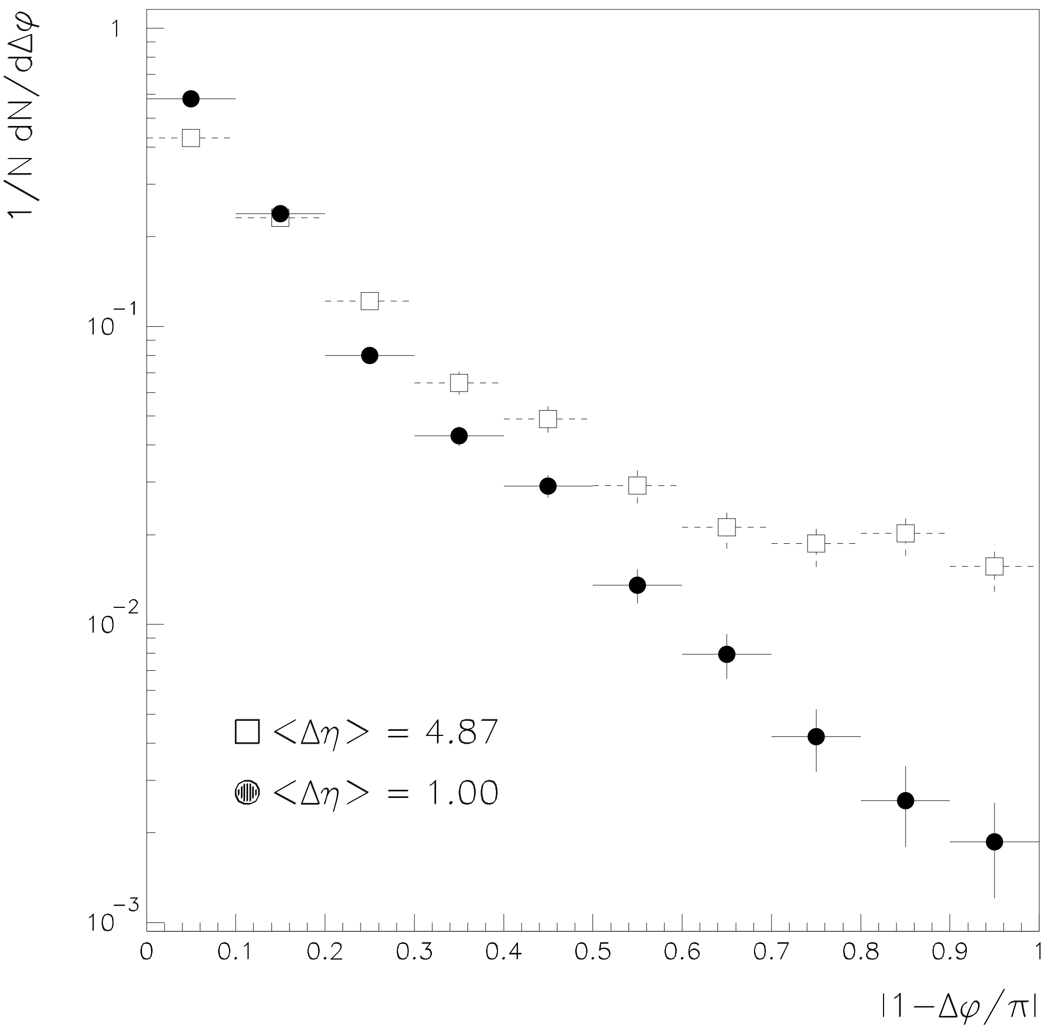

Figure 5.8: The azimuthal angular difference ($\Delta\phi = \phi_1 - \phi_2$) of the two tagging jets plotted as $|1 - \Delta\phi/\pi|$ for $\Delta\eta = 1$ ($\langle\Delta\eta\rangle = 1.00$) and $\Delta\eta = 5$ ($\langle\Delta\eta\rangle = 4.87$) bins. Errors are statistical only.

5.2.3 $< \cos(\pi - \Delta\phi) >$

To quantify the decorrelation effect, we define a correlation variable $< \cos(\pi - \Delta\phi) >$, which varies from unity for the completely correlated case to zero for the completely uncorrelated one. The average of the rapidity interval in unit bins is used. As shown in figure 5.9, $< \cos(\pi - \Delta\phi) >$ decreases as $\Delta\eta$ increases, that is, the decorrelation increases with rapidity interval. The errors are statistical only; systematic errors are not included in the plot yet. The statistical error is the uncertainty in the expectation of $< \cos(\pi - \Delta\phi) >$ due to the limited statistical sample which corresponds to the root mean square divided by the square root of the total number of events in each $\Delta\eta$ bin. The $< \cos(\pi - \Delta\phi) >$ value does not approach unity as $\Delta\eta$ goes to zero since there is additional radiation outside the rapidity interval. Experimental smearing due to detector effects also causes this effect. More details of the $\Delta\phi$ distribution could be resolved by the n^{th} moment of the decorrelation variable ($< \cos[n(\pi - \Delta\phi)] >$). The choice of decorrelation variable is arbitrary and can be replaced by any definition that describes the partial degree of decorrelation without ambiguity. An alternative definition for a decorrelation variable for this analysis is described elsewhere [29].

5.3 Corrections and Systematics

Measuring the decorrelation of the two jets involves many experimental and systematic corrections introduced by the intrinsic inaccuracies of the detector. There are three main categories of experimental factors which contribute to corrections and systematics: 1) biases due to event selection requirements, 2) inaccuracies in measuring the properties of jets, and 3) other sources of mistagging the two jets in events such as reconstruction inefficiency and jet quality cuts. In this section, we will study the necessary corrections and important experimental systematics, especially focusing on the measurement of $< \cos(\pi - \Delta\phi) >$.

Throughout this analysis, the imposition of a minimum E_T requirement, typically

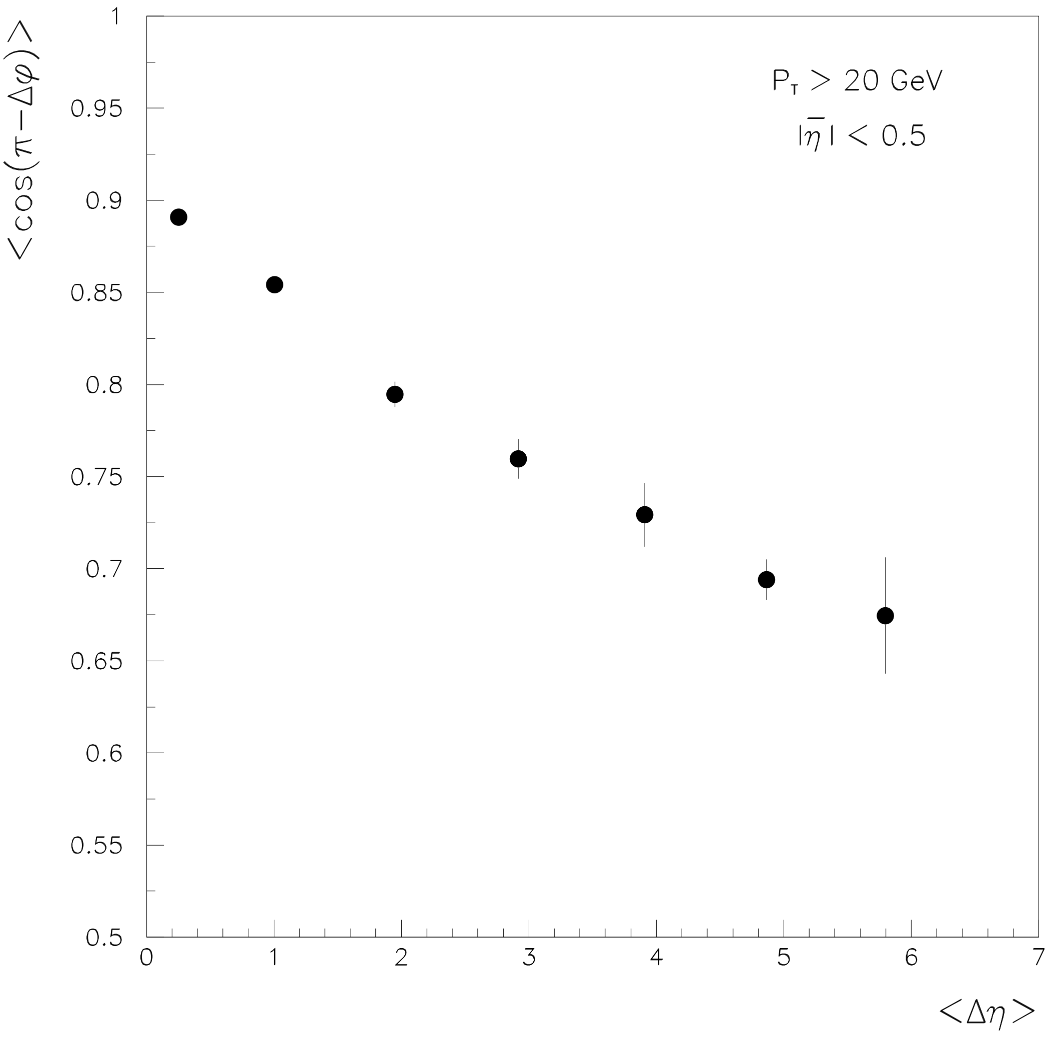

Figure 5.9: The azimuthal decorrelation variable used in this analysis, the average of $\cos(\pi - \Delta\phi)$ (uncorrected), as a function of $\Delta\eta$.

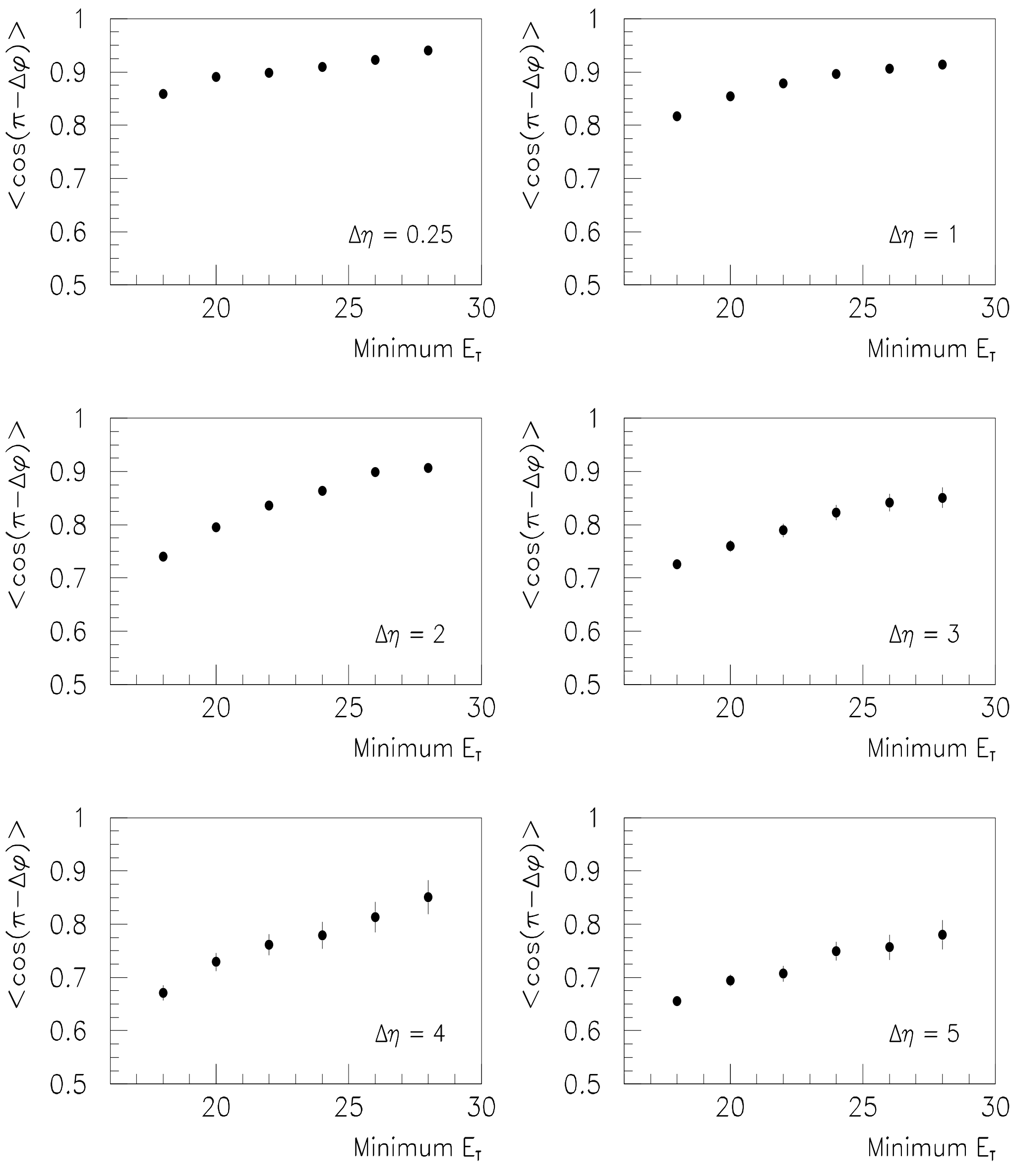

Figure 5.10: The dependence on the minimum E_T of the jet on $< \cos(\pi - \Delta\phi) >$ for each $\Delta\eta$.

20 GeV, on our jet definition plays a central role in both the measurement of the decorrelation effect as well as in the determination of the systematic uncertainties. As shown in figure 5.10, a lower E_T threshold results in a stronger decorrelation effect. This behaviour coupled with three aspects of jet measurements, trigger threshold, energy scale correction, and jet energy resolution, may result in systematic biases in the decorrelation measurement. Any trigger inefficiency resulting in a preferential loss of jets at lower E_T would result in a measurement biased high. An incorrect energy scale correction could bias the decorrelation measurement either high or low depending on the direction of the correction. The rapidly falling jet cross section, when combined with the finite jet energy resolution could produce a lower decorrelation measurement as the cross section provides more low E_T jets to fluctuate high than high E_T jets to fluctuate low. All three aspects of jet measurements need to be studied and understood in order to determine the necessary corrections to produce an unbiased measurement of the azimuthal decorrelation. For convenience sake, we will refer to $<\cos(\pi - \Delta\phi)>$ as $< \cos\Delta\phi >$ in the rest of this chapter.

5.3.1 Trigger Inefficiencies

The corrections to the measured value of $< \cos\Delta\phi >$ for any trigger inefficiencies are determined by varying the minimum E_T cutoff. This correction factor will always be negative since, as stated above, any trigger inefficiency will result in the preferential loss of lower E_T, more decorrelated, jets. Knowing the event trigger efficiency $\epsilon(E_{T1}, E_{T2}, \Delta\eta)$ and the event tagging jet probability density $\omega(E_{T1}, E_{T2}, \Delta\eta)$, we can write the correction due to trigger inefficiency as

$$\begin{aligned} \delta < \cos\Delta\phi > (\Delta\eta) &= \int dE_{T1} dE_{T2} \omega < \cos\Delta\phi > (1 - \frac{1}{\epsilon}) \\ &\approx \sum_{i=bins} \omega_i < \cos\Delta\phi >_i (1 - \frac{1}{\epsilon_i}). \end{aligned} \tag{5.11}$$

For this study we use nine bins in the region 20 GeV $< E_{T1}(E_{T2}) <$ 29 GeV and assume that the trigger is 100% efficient for $E_T >$ 29 GeV. Within a reasonable approximation, we can use the data distributions in E_{T1} and E_{T2} to approximate $\omega \approx \omega_i = N_i/N$ and $\epsilon \approx \epsilon_i =< \epsilon >$ for each $\Delta\eta$ where N_i is the number of events in the i^{th} bin, N is the total number of events, and $< \epsilon >$ is the average of ϵ in each E_T bin. A second iteration can be done after the first iteration has been corrected, but the size of the second correction is negligible. The size of the overall correction is $\mathcal{O}(3 \times 10^{-3})$ and contributes ~ 4 % to $< \cos\Delta\phi >$.

Even though the single jet trigger efficiency is not fully efficient near the tagging jet E$_T$ threshold, the dijet requirement for the single jet trigger sample gives very efficient event samples as either jet can satisfy the trigger: $\epsilon(E_{T1}, E_{T2}) = \epsilon(E_{T1}) + \epsilon(E_{T2}) - \epsilon(E_{T1})\epsilon(E_{T2})$. For this study, we use the average event trigger efficiency as a function of the leading E_T jet as described in section 3.3. For the JET_12_QNT trigger, the average of ϵ is greater than 98% in each $\Delta\eta$ bin for dijet events used for this analysis. The uncertainty of the correction has been considered by varying the average trigger efficiency for each $\Delta\eta$ bin within the root mean square of $< \epsilon >$, but the size of maximum errors are $\mathcal{O}(1 \times 10^{-3})$. The correction value and its uncertainty for each $\Delta\eta$ is summarized in table 5.2.

5.3.2 Reconstruction Inefficiencies

Jet reconstruction inefficiencies, a concern only for the tagging jets in the event, has the effect of changing the resulting event configuration. Nonetheless, the correction due to jet reconstruction inefficiency is rather small for this analysis due to the characteristics of this analysis. In the case of dijet events, any inefficiency causes the entire event to be discarded. Since most of samples used are dijet events, the dominant effect due to jet reconstruction inefficiency is just a statistical loss. In multijet events, the inefficiency must affect one of the tagging jets to change the event configuration. Such events must then still pass the boost cut($|\bar{\eta}| < 0.5$) to remain in the sample. In addition, the relative populations of the $\Delta\eta$ bins minimizes the effect due to changes of event configuration. Any loss of a tagging jet will result in a smaller $\Delta\eta$

where statistics are relatively larger so that the average contribution is small. The contribution to $< \cos\Delta\phi >$ due to the reconstruction inefficiency is expected to be negative since the $\Delta\phi$ distribution of mistagged events, in reality having a larger $\Delta\eta$, is more likely random.

The correction to $< \cos\Delta\phi >$ is determined by using a particle level HERWIG simulation. We first parameterize the particle jet reconstruction efficiency as a function of E_T and η by matching the particle jets to the calorimeter jets within $\Delta R = 0.5$ after GEANT and RECO, as described in section 3.4. The effect of the reconstruction inefficiency is then simulated by dropping jets randomly based on the parameterized reconstruction efficiencies. Errors on $< \cos\Delta\phi >$ are extracted as follow:

$$\delta < \cos\Delta\phi > = < \cos\Delta\phi >_{data} \frac{< \cos\Delta\phi >_H}{< \cos\Delta\phi >_{H\otimes\epsilon(E_T,\eta)}}. \tag{5.12}$$

where $< \cos\Delta\phi >_H$ is determined from the HERWIG particle level sample and $< \cos\Delta\phi >_{H\otimes\epsilon(E_T,\eta)}$ from the same sample after simulation of the reconstruction efficiency. The size of the correction is small, as expected, and is listed in table 5.2. The uncertainty in the correction is determined by varying the matching criterion used to determine the reconstruction efficiency from $\Delta R = 0.3$ to $\Delta R = 0.7$.

5.3.3 Multiple Interactions

Events from multiple interactions completely lose the true decorrelation information if each tagging jet is selected from two different events simultaneously occurring during a $p\bar{p}$ collision. Even though QNT data were taken at low luminosity with the single interaction requirement at LØ, there is an indication of multiple interactions in the total energy distribution deposited in the calorimeter as shown in figure 5.12. The distribution of data having a long tail extending well above the center of mass energy is quite different from a Gaussian-like distribution from a detector simulated HERWIG sample. Assuming that the E_TOT distribution is a Gaussian, we estimate the percentage of multiple interactions in the final event set by fitting the distribu-

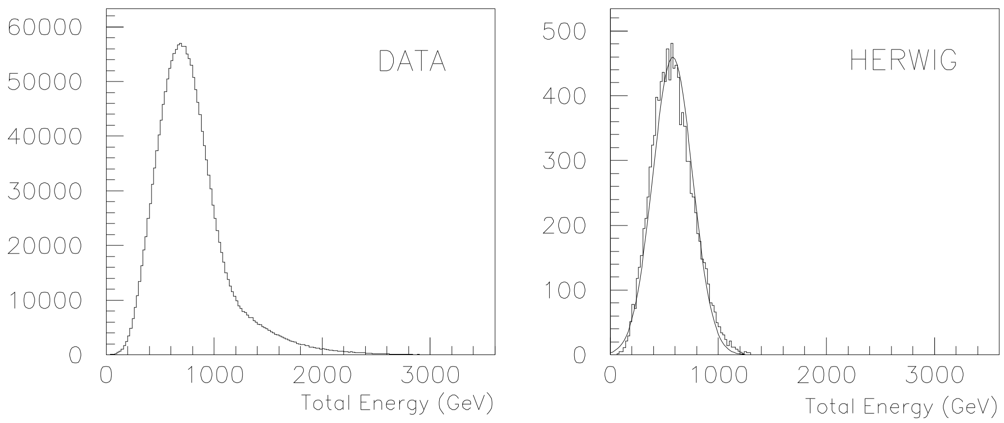

Figure 5.11: The total energy distribution for data and a detector simulated HERWIG sample. The distribution from HERWIG is fitted with a Gaussian.

tion with two Gaussian functions for each $\Delta\eta$ bin. The rate of multiple interactions among single interaction events is then obtained by dividing the area under the second Gaussian by the total area of the distribution. The area below $E\_TOT < 1800$ GeV is only used for this estimation since events having $E\_TOT > 1800$ GeV were already rejected in the event selection. Since the true E_TOT distribution may not be a Gaussian, but a smooth decreasing function terminating at $E\_TOT = 1800$ GeV, we fit the distribution with an exponential function as an alternative way to estimate the rate of multiple interactions. The average value of these two fits is used for the correction and the difference between the two fits is attributed to the uncertainty of the correction. With $< \cos\Delta\phi >$ values from multiple interaction events ($< \cos\Delta\phi >_{MITOOL=4}$) for each $\Delta\eta$ bin, we can write the true $< \cos\Delta\phi >$ as

$$< \cos\Delta\phi >= \frac{1}{1-p}(< \cos\Delta\phi >_{measured} - p\times < \cos\Delta\phi >_{MITOOL=4}), \quad (5.13)$$

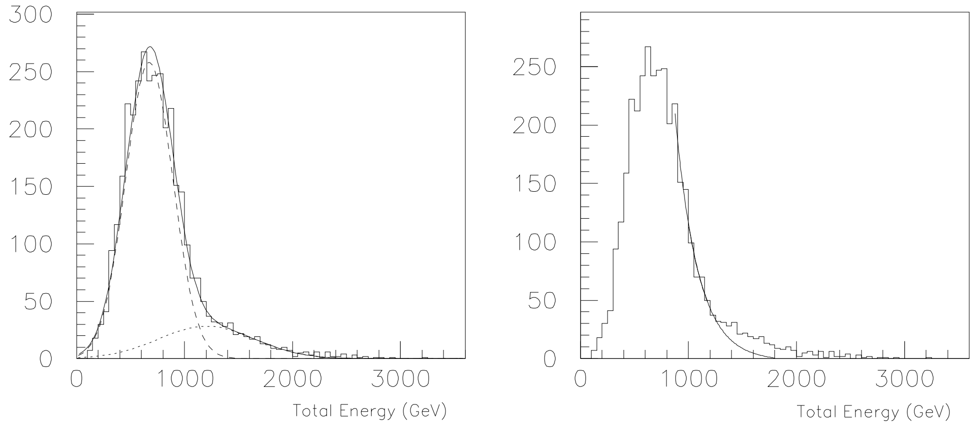

Figure 5.12: The total energy distribution for $\Delta\eta = 2$: The left plot is fitted with two Gaussian functions and the right with an exponential function. The area under the smaller Gaussian (above the exponential curve) contributes as a maximum (minimum) contamination due to multiple interactions.

$\Delta\eta$	p (%)	$< \cos\Delta\phi >_{MITOOL=4}$	$\delta < \cos\Delta\phi >$
0.25	6.1 ± 3.3	$0.678 \pm .070$	0.014 ± 0.008
1	5.7 ± 3.3	$0.509 \pm .074$	0.021 ± 0.012
2	10.4 ± 4.9	$0.225 \pm .071$	0.066 ± 0.028
3	9.5 ± 2.1	$0.417 \pm .078$	0.036 ± 0.007
4	7.3 ± 1.5	$0.364 \pm .097$	0.029 ± 0.006
5	9.1 ± 2.9	$0.306 \pm .054$	0.038 ± 0.011
6	8.8 ± 1.2	$0.277 \pm .131$	0.039 ± 0.005

Table 5.1: Summary of systematic errors due to multiple interactions.

where p is the fraction of multiple interactions among the most likely single interaction events. Since the shift due to multiple interactions is negative, the true $< \cos\Delta\phi >$ values are always greater than the measured values. The estimated p and corrections are summarized in table 5.1.

5.3.4 $\not{E}_T$ Cut and Jet Quality Cut Inefficiencies

The $METFR$ cut is designed to reject bad events mainly contaminated by cosmic rays and other localized noise activities. The $METFR$ distribution for high E_T jet triggers usually shows a noise peak at $METFR < 1.4$. As shown in figure 5.1, the distribution for samples used with the relatively low E_T jet trigger does not have a clear noise peak so that the cut may not be necessary for this analysis. However, as discussed in section 5.1.3, there is still an indication of contamination in the non-flat ϕ distribution of the leading E_T jet for events whose $METFR < 1.4$. Since the $\not{E}_T$ cut may also restrict the decorrelation contributed by undetected soft radiation, the difference of $< \cos\Delta\phi >$ with and without $E_T^{leading} / \not{E}_T > 1.4$ is accounted for as a maximal uncertainty imposing this cut, and values are listed in table 5.2.

Jet quality cuts remove not only spurious jets on a jet by jet basis from an event, but also approximately 2% of real jets due to inefficiencies of the cuts as shown in figure 4.5. Similar to reconstruction inefficiencies, this affects the measurement of the decorrelation for events having more than two jets. Events having originally only two jets will not be affected by the loss of jets because of the dijet requirement for the analysis. For all $\Delta\eta$ bins, the size of this systematic error is small since the fraction of events having more than two jets is less than 35% (the largest is for $\Delta\eta = 6$) and the overall efficiency of jet quality cuts is greater than 98%. Furthermore, only the loss of one of the two tagging jets will contribute to this systematic and new tagging jets must meet the boost cut. Even if the remaining jets pass all selection cuts, the contribution to $< \cos\Delta\phi >$ may not be significant since the resultant $\Delta\eta$ is likely to shift to smaller $\Delta\eta$ where the number of events is higher. Unlike the systematic study for the reconstruction inefficiency, there is no simple way to simulate the effect because the particle level Monte Carlo does not have jet quality information. The size of the effect on $< \cos\Delta\phi >$ will be smaller than that due to reconstruction inefficiencies because of the better overall efficiency of jet quality cuts and an additional cut rejecting events having more than two bad jets.

5.3.5 Jet Energy Scale Uncertainties

The systematics due to jet energy scale corrections near the minimum jet E_T (20 GeV) is important for this analysis since the $< \cos\Delta\phi >$ is sensitive to the E_T threshold cutoff. Artificial changes in jet E_T due to jet energy scale uncertainties may yield a different tagging dijet configuration as well as shifting the $\Delta\eta$ for a given event. The statistics and the resultant $\Delta\eta$ will always be equal or greater (smaller) for the high correction (the low correction). The relative change in $< \cos\Delta\phi >$ is expected to be negative for the high correction and positive for the low correction, which is inferred by its dependence on the E_T threshold cutoff.

We applied the CAFIX V5.1 [23] to correct the jet energy for this analysis. As shown in figure 5.13, systematic shifts from the nominal correction are taken as the uncertainties of energy scale corrections for high and low correction on each $\Delta\eta$ bin. From the plot, the systematic shift for the high correction is larger than that for the low correction which may be due to the asymmetry in the average correction factor, which mainly comes from asymmetric errors of the MPF fit in CAFIX V5.1. Average correction factors with η near the E_T threshold for the data set used are shown in figure 5.14. The bump around $\eta = \pm 1.5$ is due to the η dependence correction in the ICD vicinity and one around $\eta = \pm 2.7$ is due to the out-of-cone showering correction which increases up to $|\eta| = 2.7$. The rapidly falling of the average correction factor at $|\eta| > 2.7$ is mainly due to the fact that the showering correction is smaller for higher jet energy while it is constant in η at $|\eta| > 2.7$ for the same jet E_T. The systematic shifts due to the out-of-cone showering correction are also listed in table 5.2.

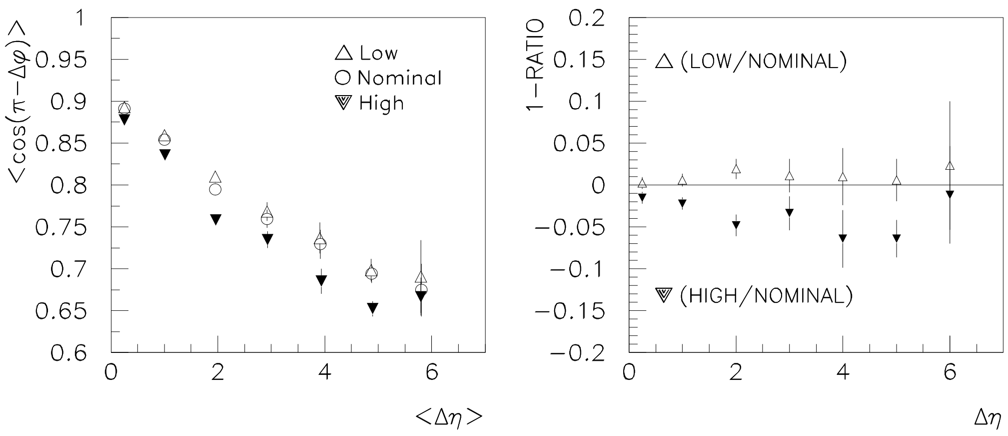

Figure 5.13: The systematic shift due to energy scale correction.

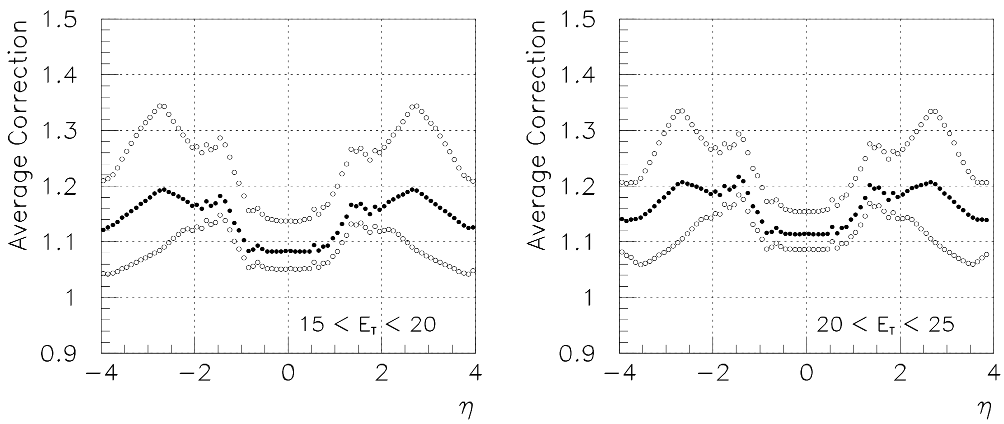

Figure 5.14: The average correction factors as a function of η. Closed circles represent the nominal correction and open ones represent the range of correction uncertainties.

5.3.6 Jet Energy Resolution

The intrinsic detector energy resolution affects the analysis when combined with the rapidly falling cross section of the tagging jet E_T . The worse E_T resolution for lower E_T jets and the falling E_T cross section generally produce more fluctuations of jets from lower to higher E_T bins. Since $< \cos\Delta\phi >$ for the relatively lower E_T scale is smaller, this yields a negative systematic shift on $< \cos\Delta\phi >$. The exact correction due to the jet energy resolution is a matter of an unsmearing procedure in the quadratic cross section $d^4\sigma/dE_{T1}dE_{T2}d\Delta\eta d\bar{\eta}$. To obtain the overall correction to $< \cos\Delta\phi >$, we need to know the unsmeared quadratic cross section, $< \cos\Delta\phi >$, and the jet E_T resolution well below the tagging jet E_T threshold. Furthermore it is also very difficult to extract systematic effects for the event migration in $\Delta\eta$ bins after the dijet event configuration changes due to the jet energy resolution.

The effect due to the jet energy resolution is alternatively determined by a Monte Carlo simulation. We parameterize the particle jet E_T resolution by comparing the particle jet E_T to the calorimeter jet E_T as a function of the particle jet E_T and η as shown in figure 4.2. The energy resolution for particle jets is then used for parameterizing a simple smearing function for a resolution simulation. Again the correction to $< \cos\Delta\phi >$ is determined by the fractional difference between the particle level sample and its resolution simulated sample:

$$\delta < \cos\Delta\phi > = < \cos\Delta\phi >_{data} \frac{< \cos\Delta\phi >_H}{< \cos\Delta\phi >_{H\otimes S(E_T,\eta)}}, \tag{5.14}$$

where $< \cos\Delta\phi >_{H\otimes S(E_T,\eta)}$ is determined from the convolution of a smearing function, $S(E_T,\eta)$, on the same HERWIG sample. The correction uncertainty is estimated by taking into account the uncertainty of jet energy resolution.

5.3.7 Jet Position Resolution

Errors on $< \cos\Delta\phi >$ due to the position resolution in the jet finding are semi-analytically determined by using the event distribution in the $\Delta\eta - \Delta\phi$ space. Within a first order approximation, it is assumed that the normalized event distribution, $f(\Delta\eta, \Delta\phi)$, is the true probability distribution of the dijet events in the given $\Delta\eta - \Delta\phi$ configuration. By definition, we can write

$$< \cos\Delta\phi > (\Delta\eta, \Delta\phi) = \int d\Delta\eta \int d\Delta\phi f(\Delta\eta, \Delta\phi) \cos\Delta\phi(\Delta\eta, \Delta\phi). \qquad (5.15)$$

The $\Delta\eta$ and $\Delta\phi$ resolution is parameterized by the η and ϕ resolution of the two tagging jets with a simple relation: $\sigma_{\Delta x} = \sqrt{\sigma_{x1}^2 + \sigma_{x2}^2}$. Errors due to the $\Delta\eta$ and $\Delta\phi$ resolution are then obtained separately by a variational method using the probability distribution. Assuming that the ϕ resolution does not depend on ϕ and using partial integration, we obtain the errors due to $\Delta\phi$ and $\Delta\eta$ resolution:

$$\begin{aligned} \delta < \cos\Delta\phi >_{\Delta\phi} &\approx < \sigma_{\Delta\phi}^2 \cos\Delta\phi >, & (5.16)\\ \delta < \cos\Delta\phi >_{\Delta\eta} &\approx < \sigma_{\Delta\eta} > \frac{d < \cos\Delta\phi >}{d\Delta\eta}, & (5.17) \end{aligned}$$

where we use the average $\sigma_{\Delta\eta}$ and the measured $< \cos\Delta\phi >$ to calculate its slope in $\Delta\eta$ for each $\Delta\eta$ bin. The physical interpretation of these errors is quite straight forward. Since the $\Delta\phi$ distribution is symmetric, the leading contribution comes from the second variation for the fluctuation of the azimuthal angle difference. On the other hand, the error due to the η resolution takes account of the event migration near boundaries of each $\Delta\eta$ bin combined with the non-zero slope of $< \cos\Delta\phi >$.

5.3.8 Jet Algorithm

For this analysis, we use the Snowmass jet algorithm described in chapter 3.3. The DØ experiment has historically used the DØ angle definition to determine the η and ϕ position of the jet:

$$\eta^{jet} = -\ln\tan(\frac{\theta}{2}), \qquad \phi^{jet} = \tan^{-1}(\frac{E_x}{E_y}), \qquad (5.18)$$

where $\theta = \tan^{-1}(\sqrt{E_x^2 + E_y^2}/E_z)$ and E_i is defined in equation 3.5. To avoid any ambiguity of the choice of jet algorithm, we compare values of $< \cos\Delta\phi >$ for the

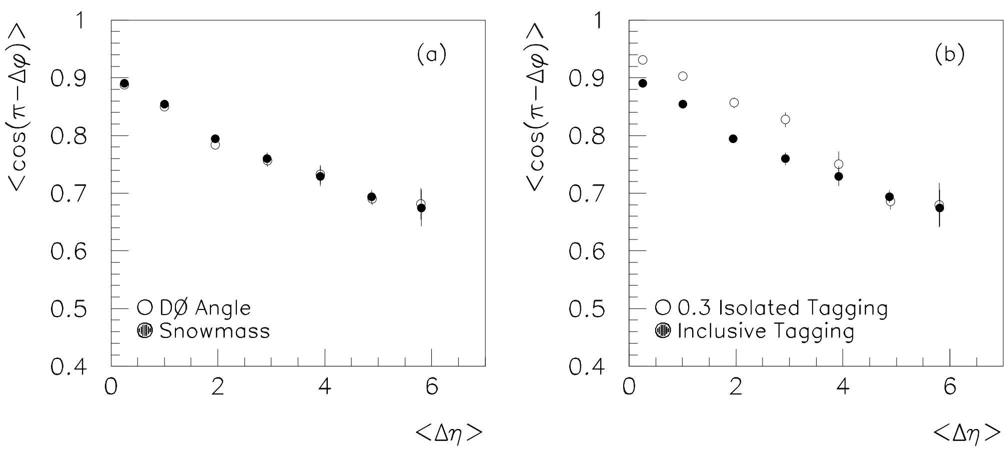

Figure 5.15: The dependence on jet algorithm and isolated tagging techniques.

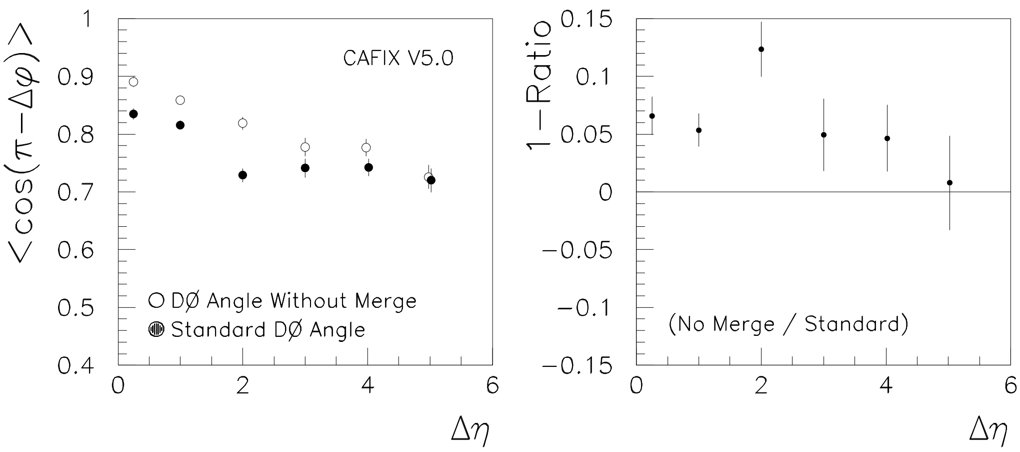

Figure 5.16: The dependence of merged and split in the DØ angle algorithm.

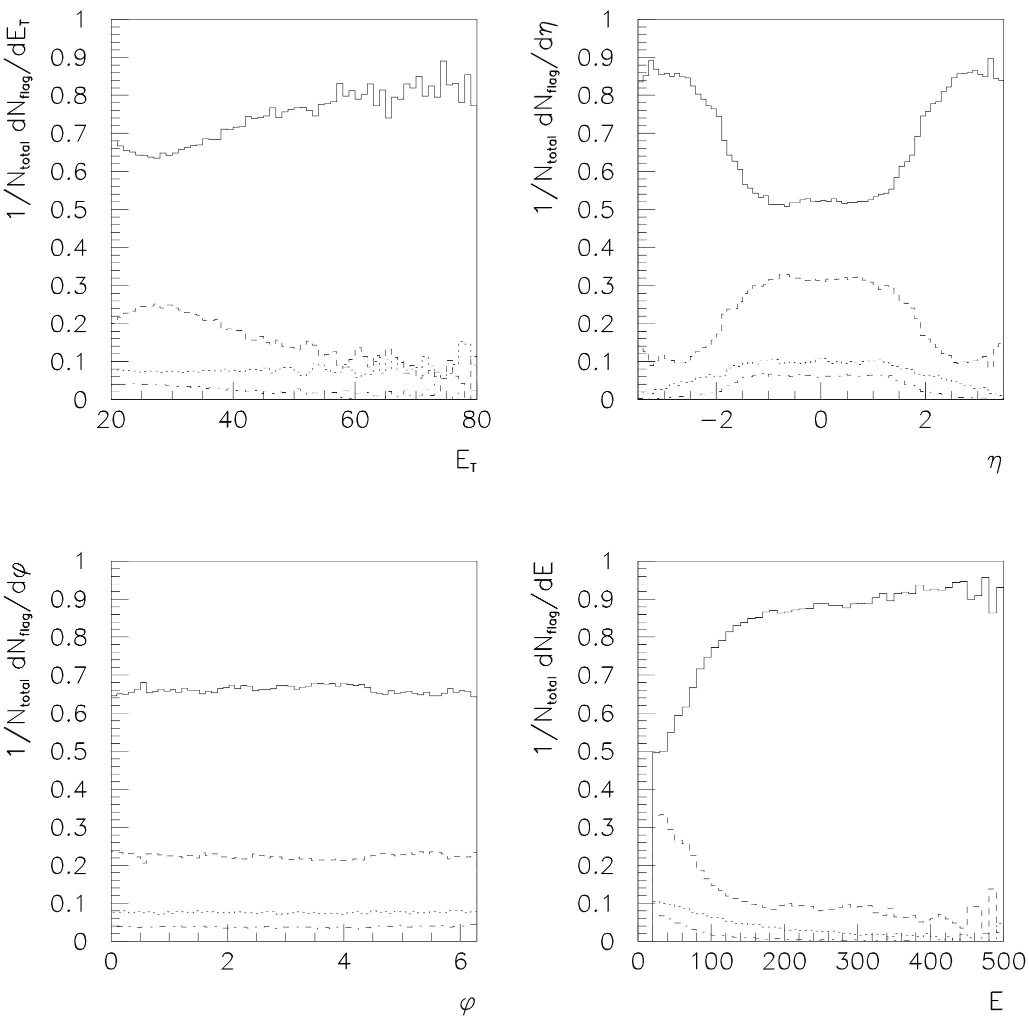

Figure 5.17: The merged and split fraction of jets by E_T, η, ϕ, and energy of jets. From top to bottom, each line represents the fraction of isolated jets, merged jets, split jets, and complicated jets.

two algorithms. As shown in figure 5.15.(a), there is no significant difference on $< \cos\Delta\phi >$ between the two algorithms.

The biggest variation of $< \cos\Delta\phi >$ in small $\Delta\eta$ bins is caused by jet merging and splitting since low E_T jets in the central detector region are more likely merged and split as shown in figure 5.17. The variation is totally jet algorithm dependent, and can not be avoided as long as we use the fixed cone algorithm. Figure 5.15.(b) shows $< \cos\Delta\phi >$ when selecting only isolated tagging jets, which indicates pairs of merged or split jets to be more likely decorrelated. Important variables of this analysis are the minimum E_T cutoff as well as tagging jet positions. With the jet algorithm, merged jets must behave like isolated jets in E_T and direction while split jets are characterized by higher order process. An essential systematic difference between isolated and merged jets is in the E_T distribution which should be the same if the algorithm works perfectly. There exists a relative over-abundance near $E_T \sim$ 30 GeV for merged jets in the E_T distribution. This bias may be due to the minimum jet reconstruction E_T which gives a relatively higher threshold for the merged jet E_T.

To understand the characteristics of merged jets better, we reconstructed part of the sample without merging or splitting jets. The ratio of $< \cos\Delta\phi >$ as well as $< \cos\Delta\phi >$ is shown in figure 5.16. For this study, we used the DØ angle algorithm with CAFIX V5.0 [22]. Without merging jets, the decorrelation pattern especially at small $\Delta\eta$ is significantly different. However we will leave this as an open question since it is not really clear whether this difference is inherent from the jet algorithm itself or from the energy scale corrections which were only parameterized for the standard DØ angle algorithm. The BFKL calculations [16, 10] are only at the parton level, where the tagging jets are single partons. The radiation in between the two jets in η is integrated right up to the η of each tagging jet excluding radiation in a cone of $R = 0.7$ around the two tagging jets, but it is never merged with the tagging jet. Nonetheless this is only important at small $\Delta\eta$ where the BFKL calculation may not be very accurate anyway.

5.3.9 Miscellaneous Systematics

There is a known reconstruction η bias in jet psuedorapidity [26]. The psuedorapidity dependence of the geometrical calorimeter tower size along with the jet algorithm is mainly responsible for a tendency to shift the reconstructed jet η toward the central region. Therefore the resultant corrected $\Delta\eta$ ($\equiv \Delta\eta_c$) for the tagging jets is always larger than the measured $\Delta\eta$, that is, $\Delta\eta_c = \Delta\eta + b$ where b is a positive function of the tagging jet η and energy. The largest b is ~ 0.1 in $\Delta\eta = 6$. Since the slope of $< \cos\Delta\phi >$ in $\Delta\eta$ is negative, this η bias correction yields a positive correction to values of $< \cos\Delta\phi >$ which is listed in table 5.2.

The event acceptance for $\Delta\eta = 6$ is not 100% due to the maximum $|\eta|$ cut ($|\eta| < 3.5$) as shown in figure 5.4. Instead of $|\eta| < 3.75$ for the full event acceptance, the cut is introduced to avoid significant problems for reconstructing and triggering jets at $|\eta| > 3.5$ where jets are more likely to be contaminated by the beam activity. This partial acceptance for the last $\Delta\eta$ bin may not impair the measurement because the data is shown with the average of $\Delta\eta$ of the observed events. With $|\eta| < 3.75$, there is no difference on $< \cos\Delta\phi >$ in $\Delta\eta = 6$ with 0.002 change on $< \Delta\eta >$. For samples used, only two more events are found in $\Delta\eta = 6$ with the cut and one event is lost in $\Delta\eta = 0.25$ since it failed the $\bar{\eta}$ cut. In general the analysis is also insensitive to the maximum $|\eta|$ cut above 3.75 where jets with $E_T > 20$ GeV are kinematically suppressed with the fixed center of mass energy of the Tevatron. The $|\eta|$ cut has been varied up to the jet reconstruction limit in η ($|\eta| = 4.2$), but there are no changes in values of $< \cos\Delta\phi >$ and the number of events in every $\Delta\eta$ bin.

Since jets are more likely merged or split in the central region, there is also a dependence on the $\bar{\eta}$ cut of the decorrelation at small $\Delta\eta$ bins. As shown in figure 5.18.(a), the decorrelation of jets at large $|\bar{\eta}|$ where most of jets are isolated jets is relatively stronger. For this study we only use events from the inclusive trigger not to overweigh events having the same side two jets at large $\Delta\eta$ from the forward trigger. Without the $\bar{\eta}$ cut, values of $< \cos\Delta\phi >$ at $\Delta\eta \leq 4$ highly depend on the

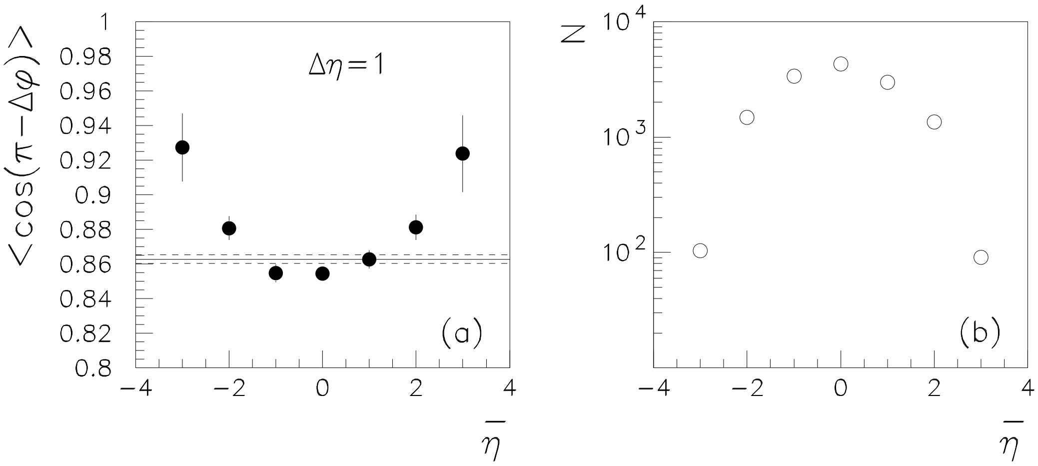

Figure 5.18: The dependence on the $\bar{\eta}$ for $\Delta\eta = 1$: Lines represent the average of $< \cos(\pi - \Delta\phi) >$ with statistical error bands.

number of events from the forward trigger. We list the difference of $< \cos\Delta\phi >$ between $|\bar{\eta}| < 0.5$ and $|\bar{\eta}| < 3.5$ (no $\bar{\eta}$ cut with $|\eta| < 3.5$) in table 5.2. With only the inclusive trigger, the dependence of the $\bar{\eta}$ cut will be much smaller since events are highly populated at small $|\bar{\eta}|$ as shown in 5.18.(b).

5.3.10 Summary of Errors and Systematics

A summary of corrections as well as the statistical and systematic errors of $< \cos\Delta\phi >$ for each $\Delta\eta$ are shown in table 5.2. Corrections will be applied to determine the final values of $< \cos\Delta\phi >$. These include corrections for the trigger inefficiency, the reconstruction inefficiency, the jet energy resolution, and multiple interactions. We will not include the correction for the η bias since the definition of parton jets is experimentally rather arbitrary. The correction for multiple interactions dominates other corrections and the biggest correction is $\sim 8\%$ at the $\Delta\eta = 2$ bin. Significant

$< \Delta\eta >$	0.25	1.00	1.95	2.92	3.92	4.87	5.81
$< \cos(\pi - \Delta\phi) >$	0.891	0.854	0.795	0.760	0.729	0.694	0.675
statistics	2143	4285	3443	1694	681	1980	262
statistical error	0.004	0.004	0.007	0.011	0.017	0.011	0.032
trigger inefficiency (c)	-0.003	-0.003	-0.002	-0.002	-0.002	-0.003	-0.003
RECO inefficiency (c)	0.000	0.001	0.001	0.001	0.001	0.004	-0.004
E_T resolution (c)	0.014	0.016	0.013	0.011	0.007	0.004	-0.001
mutiple interactions (c)	0.014	0.021	0.066	0.036	0.029	0.038	0.039
η bias correction (c)	0.001	0.004	0.001	0.001	0.001	0.006	0.008
trigger inefficiency (us)	0.001	0.001	0.001	0.001	0.001	0.001	0.001
RECO inefficiency (us)	0.001	0.001	0.000	0.000	0.001	0.001	0.002
E_T resolution (us)	0.004	0.004	0.004	0.004	0.003	0.005	0.006
multiple interactions (us)	0.008	0.012	0.028	0.007	0.006	0.011	0.005
ϕ resolution (us)	0.002	0.003	0.002	0.001	0.002	0.002	0.002
η resolution (us)	0.002	0.002	0.002	0.002	0.002	0.002	0.002
missing E_T cut (us)	0.004	0.010	0.016	0.008	0.002	0.009	0.000
energy scale(low) (cs)	0.002	0.005	0.016	0.009	0.007	0.004	0.016
energy scale(high) (cs)	-0.013	-0.019	-0.036	-0.025	-0.044	-0.042	-0.008
out-of-cone showering (cs)	0.001	0.003	0.016	0.020	0.008	0.011	0.008
isolated jet only (cs)	0.040	0.049	0.062	0.068	0.021	-0.009	0.005
complicated jets (cs)	0.028	0.040	0.039	0.019	0.012	0.004	-0.003

Table 5.2: Summary of corrections, and statistical and systematic errors. Parenthesis (c) represents a correction, (us) an uncorrelated systematic error, and (cs) a correlated systematic error.

correction uncertainties will be included as uncorrelated systematic errors.

The largest statistical error is 4.7% for the measurement at the $\Delta\eta = 6$ bin. The systematic errors, especially the energy scale uncertainty, dominate the statistical errors for all $\Delta\eta$ bins except for $\Delta\eta = 6$. At small $\Delta\eta$ ($\Delta\eta \leq 3$), there is a significant variation in using isolated jets exclusively or complicated jets inclusively. These uncertainties are inherent in the definition of jets when they are overlapped within the cone size. We will present these as variations of the measurement, but not as experimental errors. Statistical and uncorrelated systematics errors will be added in quadrature and will be presented on each data point. The correlated systematic errors, especially due to uncertainties of the jet energy corrections, will be presented separately.

5.4 Parton Shower Monte Carlo

Jet decorrelation may also be produced via gluon emission in the parton density evolution. Many Monte Carlo event generators simulate high order QCD effects approximated by the parton showering schemes based on the DGLAP evolution and superimposed on the leading order QCD 2 to 2 parton process. In general, a parton shower Monte Carlo for high energy hadronic processes incorporates perturbative QCD cross sections, initial and final state QCD radiative corrections in LLA, hadronization models, and the underlying event. The choice of the proper event generator and its reliability depend on how a specific physics process is sensitive to detailed features of models implemented inside Monte Carlo simulations. For this analysis, we use three different parton shower event generators, HERWIG [13], PHYHIA [14], and ISAJET [15] to compare to data and a prediction based on the leading logarithmic BFKL calculation [12]. In this section, we briefly review the the physics underlying HERWIG especially related to this analysis and describe important aspects of PYTHIA and ISAJET as well as sample event generation for the analysis.

5.4.1 HERWIG

HERWIG (for Hadron Emission Radiation With Interfering Gluons) is a parton shower simulation where higher order effects are approximated by the parton shower which is superimposed on the leading order QCD 2 to 2 parton process. The main theoretical justification lies in the factorization theorem for hard processes. The higher order effects are implemented through angular ordering; radiation of each subsequent gluon is always at a smaller relative angle than the previous radiation. This will in effect resum certain types of soft gluon radiation where the resummation is governed by the DGLAP equation.

HERWIG uses the parton shower approach for initial state and final state QCD radiation including color coherence effects and azimuthal correlation both within and between jets. The intial state emission process leads to the evolution of the structure function $F(x, Q)$ of the incident hadron. In the program, this process is characterized by the choice of a parton distribution function. The elementary hard subprocess for the QCD 2 to 2 parton production is computed exactly to leading order in perturbative theory including soft gluon interferences and color connections. Then the final state emission factorizes as a successive coherent branching process of which the energy fractions are distributed according to the Altarelli-Parisi splitting functions and the full available phase space is restricted to an angular-ordered region. The emission angles are distributed according to the Sudakov form factors, which resum the virtual corrections and normalize the branching distribution to give a probabilistic interpretation needed for a Monte Carlo simulation. The azimuthal angular distribution in each branching is determined by the eikonal dipole distribution for a soft emitted gluon and azimuthal correlations due to spin effects for non-soft emission. In each branching the scale of α_s is the relative transverse momentum of the two emitted partons. The last process, hadronization, is implemented by the cluster fragmentation model which converts the emitted partons into hadrons including the incoming partons as constituents of the incident hadrons, and the underlying soft event associated with the presence of spectator partons.

HERWIG has very successfully described various jet distributions in the past including the recent DØ jet shape [30] and the previous azimuth decorrelation study [11]. Secondly we use the Monte Carlo to understand various theoretical and experimental systematic errors. For our HERWIG analysis, we use the HERWIG V5.8 with the CTEQ2M parton distribution function. We generated on the order of two million events with a minimum parton p_T (PTMIN) of 14 GeV, a maximum of 900 GeV with Λ_{QCD} = 180 GeV, and very loose constraints on the rapidity ($-8 < \eta < 8$). For clustering particle jets, the 0.7 cone with a minimum E_T of 10 GeV is used. The $< \cos \Delta\phi >$ as a function of $\Delta\eta$ is shown in figure 5.19 for HERWIG, PYTHIA, and ISAJET.

5.4.2 PYTHIA and ISAJET

PYTHIA, which has underlying physics similar to that of HERWIG, provides many possibilities for choices of color coherence effects as well as hadronization models. String fragmentation and independent fragmentation are two choices of hadronization model. Choices of color coherence effects include angular ordering for time-like showers, azimuthal distributions in gluon decays, Q^2 ordering in space-like parton shower evolution, and color coherence effects in the first branching of the backwards evolution of an initial state shower.

ISAJET, on the other hand, does not include angular ordering and other color correlations. ISAJET uses independent fragmentation for the hadronization of partons with a 6 GeV invariant mass cutoff for parton showers. The cutoff is rather large compared with the PYTHIA default value (1 GeV) because a lower cutoff would give too many hadrons from overlapping partons with independent jet fragmentation. PYTHIA and ISAJET samples are generated particularly to understand the underlying physics related to this analysis with different choices of fragmentation models, color coherence effects and invariant mass cut-off of parton showers. For this pur-

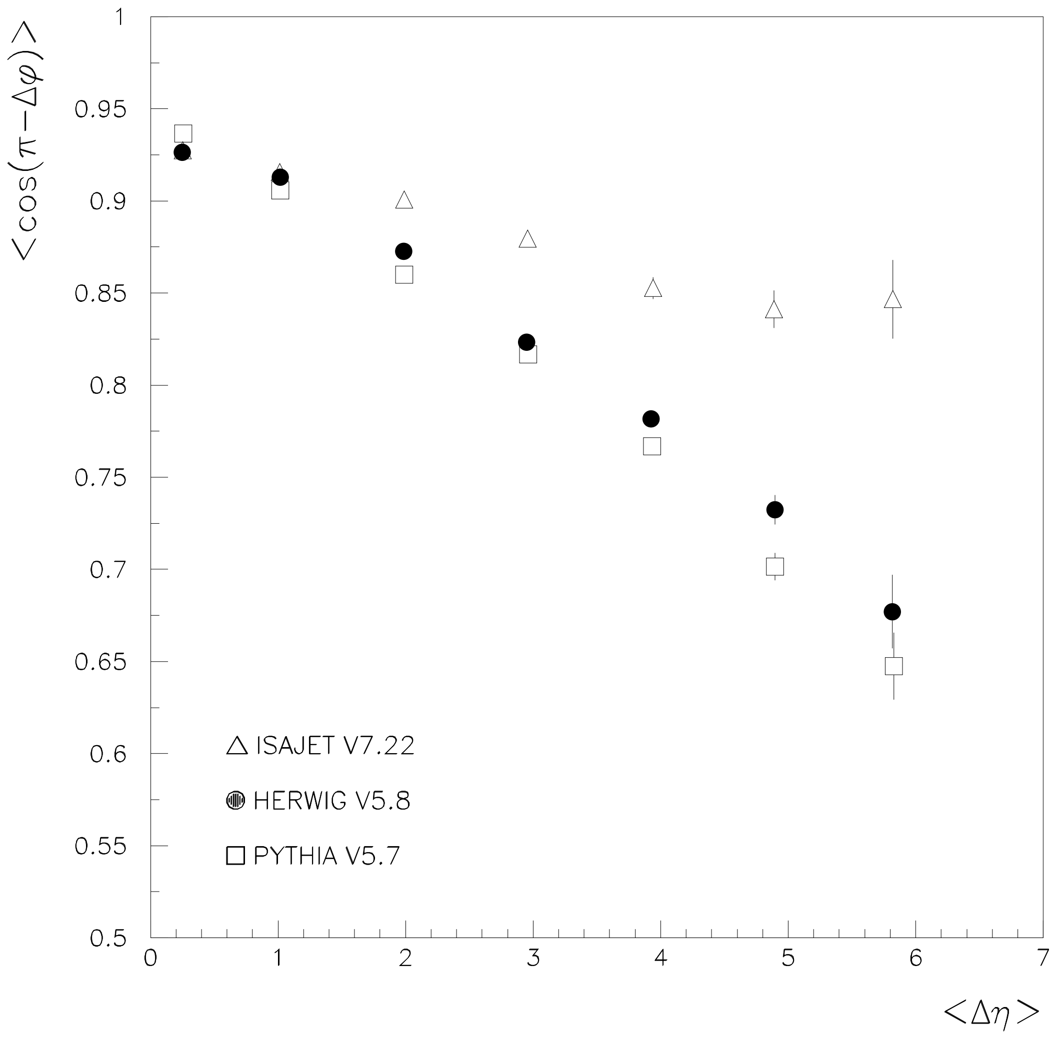

Figure 5.19: The average value of $\cos(\pi - \Delta\phi)$ as a function of $\Delta\eta$ for HERWIG, PYTHIA, and ISAJET.

Monte Carlo	HERWIG	PYTHIA	ISAJET
Version	V5.8	V5.7	V7.22
PDF	CTEQ2M	CTEQ2M	CTEQ2L
Minimum Parton P_T	14 GeV	14 GeV	14 GeV
Maximum Parton η	(-8,8)	(-8,8)	(-4,9,4.9)
Color Coherence	Default	On and Off	-
Parton Shower Mass Cut-off	2.5 GeV	1.0 GeV 6.0 GeV	6.0 GeV
Fragmentation Model	Clustering	String Independent	Independent
Underlying Event Multiple Interaction	On -	Pile-up: Off Off	On -
Cone Jet Algorithm Cone Size (R) Minimum E_T of Jet	DØ Particle Jet 0.7 10 GeV	DØ Particle Jet 0.7 10 GeV	DØ Particle Jet 0.7 10 GeV
Number of Event	$\sim 2,100,000$	$\sim 2,500,000 \times 6$	800,000

Table 5.3: Summary of parton shower Monte Carlos for the QCD 2 to 2 process.

pose, we generated four sets of PYTHIA samples with 1 GeV mass cutoff and two sample sets with 6 GeV parton shower mass cutoffs. Important features of Monte Carlo samples used for this analysis are summarized in table 5.3.

For the azimuthal decorrelation, PYTHIA with its string model and color coherence effects agrees well with HERWIG within statistical errors. Dependences on fragmentation model, color coherence effects, and the invariant mass cutoff for parton showers of PYTHIA samples are shown in figure 5.20. The dependence on hadronization model of $< \cos\Delta\phi >$ is studied by comparing results from two samples with different fragmentation models generated with all color coherence effects. The difference between string fragmentation and independent fragmentation is relatively small

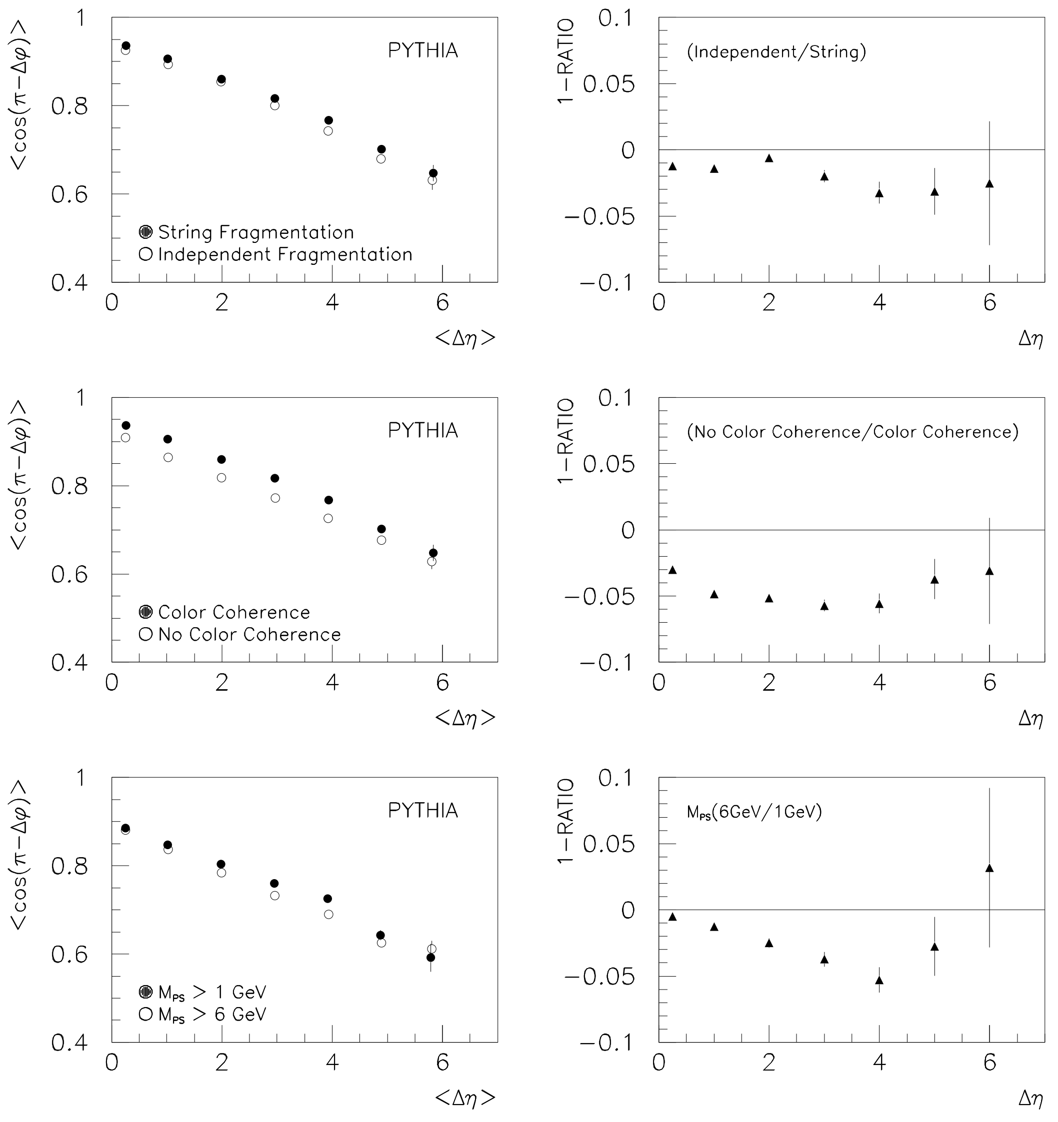

Figure 5.20: The dependence on fragmentation models, color coherence effects, and the invariant mass cutoff for parton showers of $< \cos(\pi - \Delta\phi) >$ in PYTHIA.

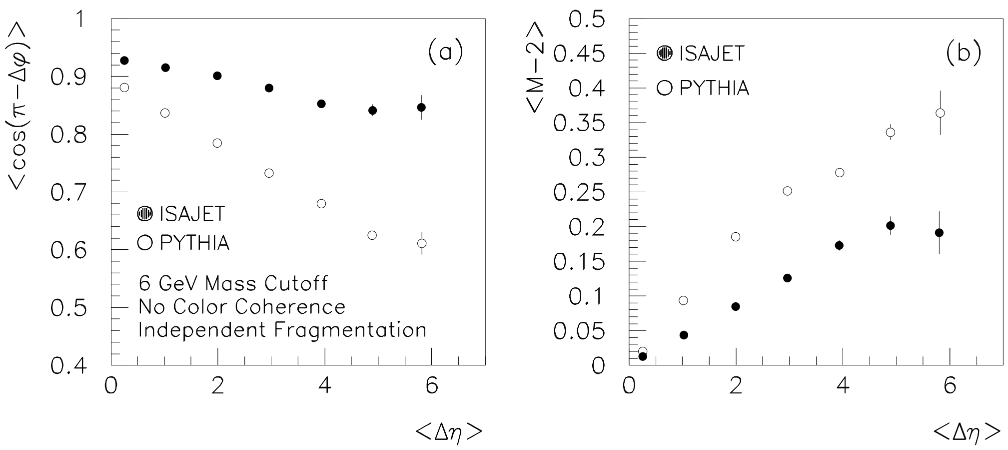

Figure 5.21: Comparisons between ISAJET and PYTHIA. (a) $< \cos(\pi - \Delta\phi) >$ with the 6 GeV mass cutoff for parton showers and independent fragmentation without color coherence effects. (b) Jet ($E_T > 20$ GeV) multiplicity as a function of $\Delta\eta$.

($\leq 3\%$) for the analysis. However, the dependence on color coherence effects is rather significant ($\leq 6\%$) on $< \cos \Delta\phi >$. The mass cutoff dependence has been checked with the choice of 1 GeV and 6 GeV mass cutoff for independent fragmentation without any color coherence.

As shown in figure 5.19, the result from ISAJET shows significantly less decorrelation as the rapidity interval increases. The best sample to compare to ISAJET is the PYTHIA sample with the 6 GeV mass cutoff and independent fragmentation without any color coherence effects. Based on figure 5.21.(a), however, the decorrelation pattern of ISAJET may not be explained by color coherence schemes since they are not implemented in ISAJET. The significant difference between ISAJET and PYTHIA is the average jet multiplicity. As shown in figure 5.21.(b), the average jet ($E_T > 20$ GeV) multiplicity of ISAJET is much less than that of PYTHIA as the rapidity interval increases, which may be responsible for the decorrelation pattern.

Chapter 6

Results and Conclusions

Motivated by recent interest in the BFKL pomeron, we measure the azimuthal decorrelation of jets widely separated in rapidity with the variable, $< \cos(\pi - \Delta\phi) >$. Within the kinematical region that we studied ($E_T > 20$ GeV and $\Delta\eta \leq 6$), we compare data to predictions based on the leading logarithmic BFKL approximation, and parton shower Monte Carlos, HERWIG and PYTHIA. We conclude and also give several remarks on the experimental measurement as well as open questions on theoretical predictions to probe BFKL dynamics and to test the BFKL resummation at the Tevatron.

6.1 Results

After applying experimental corrections to $< \cos(\pi - \Delta\phi) >$ for the data described in the previous section, we compare the data to parton showering Monte Carlos, HERWIG and PYTHIA, and an analytical prediction based on the leading logarithmic BFKL calculation. Figure 6.1 shows the correlation variable, $< \cos(\pi - \Delta\phi) >$, as a function of $\Delta\eta$, for the data, HERWIG, and the BFKL calculation of Del Duca and Schmidt [12]. The decorrelation variable, $< \cos(\pi - \Delta\phi) >$, decreases as the rapidity

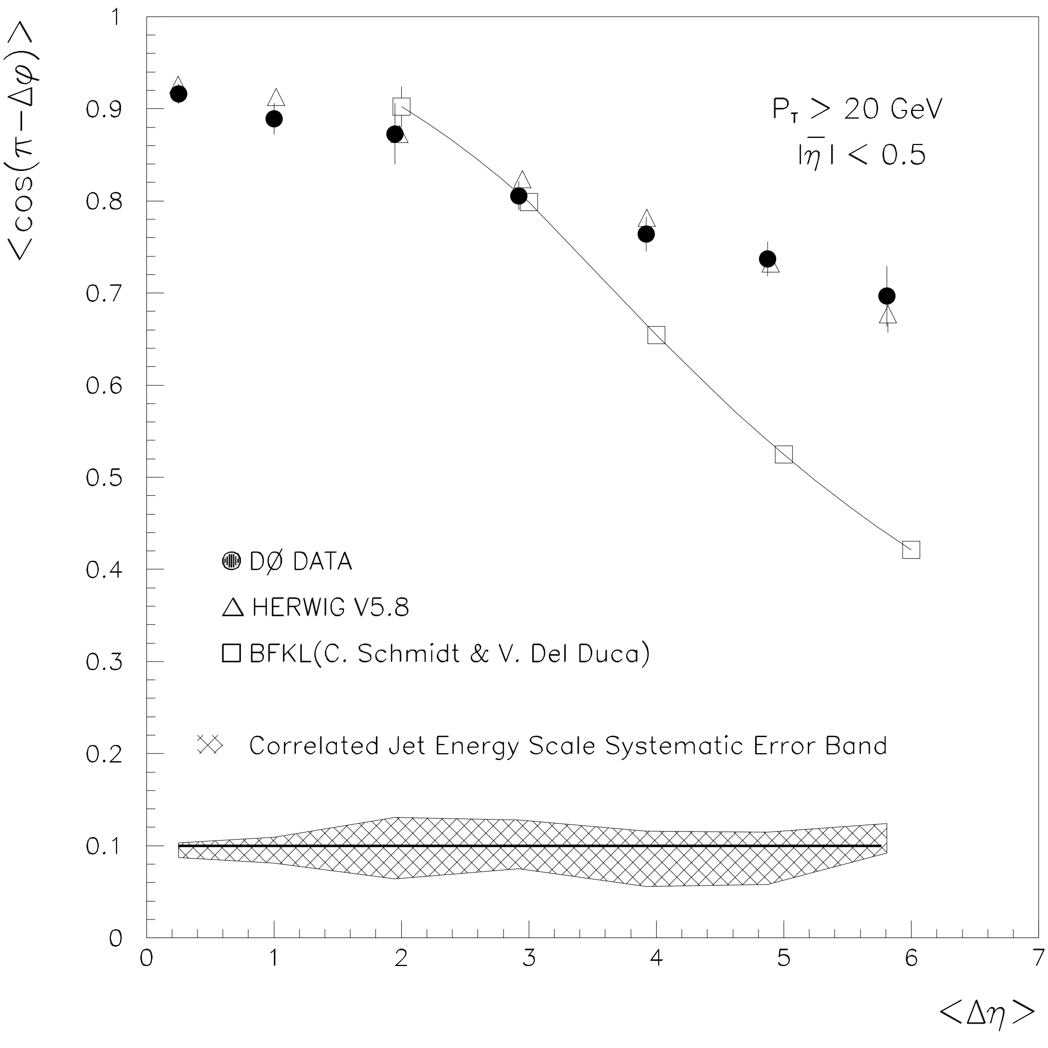

Figure 6.1: The correlation variable, $< \cos(\pi - \Delta\phi) >$, as a function of $\Delta\eta$, for the data, HERWIG, and the BFKL calculation of Del Duca and Schmidt.

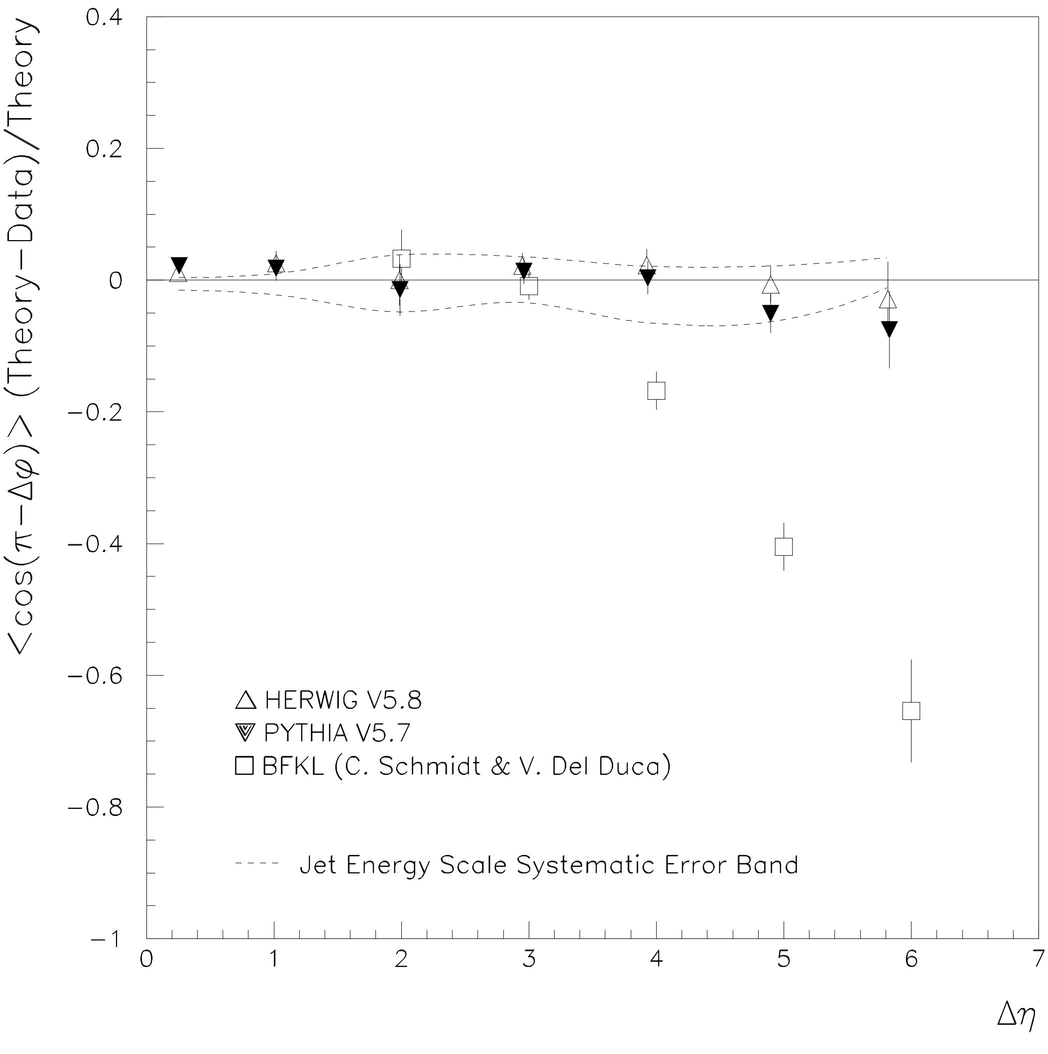

Figure 6.2: The (Theory-Data)/Theory of $< \cos(\pi - \Delta\phi) >$ as a function of $\Delta\eta$, for HERWIG, PYTHIA, and the BFKL calculation of Del Duca and Schmidt.

interval increase for the data as well as the two theoretical predictions. For the data the error bars represent the statistical and uncorrelated systematic errors added in quadrature. In addition, the band at the bottom of the plot represents the correlated uncertainties of the energy scale corrections. The CTEQ2M parton distributions [31] are used for theoretical predictions. The prediction of the leading logarithmic BFKL approximation, which is valid for large $\alpha_S \Delta\eta$, is shown for $\Delta\eta \geq 2$. Theoretical uncertainties due to the renormalization/factorization scale are not included in the BFKL calculation. The errors on the BFKL prediction are purely mathematical for the calculation. As the pseudorapidity interval increases, this calculation predicts too much decorrelation. On the other hand, the predictions based on a parton shower Monte Carlo, HERWIG, agree well with the data over the pseudorapidity interval range ($0 \leq \Delta\eta \leq 6$). Figure 6.2 shows the ratio, (Theory - Data)/Theory, for HERWIG and PYTHIA as well as the BFKL prediction. Over the entire kinematical region that we studied, predictions from HERWIG and PYTHIA agree with the data not only within $\sim 10\%$ of the measurement but also within errors of the measurement. However the prediction based on the BFKL calculation deviates linearly from $\sim 18\%$ at $\Delta\eta = 4$ to $\sim 65\%$ at $\Delta\eta = 6$.

6.2 Conclusions and Remarks

Using the variable $< \cos(\pi - \Delta\phi) >$, we measure the azimuthal decorrelation as a function of pseudorapidity separation up to $\Delta\eta = 6$ for two jets at the extremes of pseudorapidity with $E_T > 20$ GeV. These results are compared with various QCD predictions based on leading logarithmic approximations. Two parton shower Monte Carlos, HERWIG and PYTHIA, describe the data well over the entire $\Delta\eta$ range studied. The prediction based on the leading logarithmic BFKL resummation shows too much decorrelation as the rapidity interval increases.

The motivation of this analysis was to probe possible signatures of BFKL dynamics at the Tevatron. It seems that no clear signature of the BFKL pomeron has been observed within the kinematical region that we have studied. Nonetheless, there are still several open questions to be answered for the future understanding of BFKL dynamics and higher order QCD processes at the Tevatron. In the remainder of this chapter, we point out several important questions related to this measurement.

The first question relates to the validity of and the errors in the leading logarithm BFKL approximation within $2 \leq \Delta\eta \leq 6$. Consider a system having n partons ordered in rapidity ($\eta_1 \gg \eta_2 ... \gg \eta_n$) with comparable size of their transverse momenta ($p_\perp$). The leading logarithmic BFKL resummation is supposed to correct at asymptotically large $\Delta\eta$ where $\ln(\hat{s}/Q^2)$ is approximately equal to $\Delta\eta = \eta_1 - \eta_n$. Within the kinematical region that we have studied, the application of the leading logarithmic BFKL resummation may not be fully justified as one might conclude from looking at the following exact relationship for the n parton system:

$$\ln \frac{\hat{s}}{Q^2} = \ln \frac{\sum_{i=1}^{n} p_{i\perp} e^{\eta_i} \sum_{j=1}^{n} p_{j\perp} e^{-\eta_j}}{Q^2} \neq (\eta_1 - \eta_n) + \ln \frac{p_{1\perp} p_{n\perp}}{Q^2} \neq \Delta\eta. \qquad (6.1)$$

The first inequality comes from $\sum_{i=1}^{n} p_{i\perp} e^{\eta_i} \neq p_{1\perp} e^{\eta_1}$ and $\sum_{j=1}^{n} p_{i\perp} e^{-\eta_i} \neq p_{n\perp} e^{-\eta_n}$ for a moderate η_1 and η_n. The second inequality ($Q^2 \neq p_{1\perp} p_{2\perp}$) may be attributed to a uncertainty in the theoretical calculation, which has not been estimated in the BFKL calculation. Therefore the remaining question is the accuracy of the leading logarithmic BFKL resummation in the kinematical region that we studied.

A second question relates to the range and the errors inherent in the leading logarithmic BFKL approximation itself. If the size of next-to-leading corrections to the BFKL equation is large for the measurement, the current application of BFKL resummation may not be adequate to predict related quantities precisely. The calculation of the next-to-leading logarithmic corrections to the BFKL matrix elements is currently underway [32]. Furthermore, the strong coupling constant is not running in the leading logarithmic BFKL calculation which uses $\alpha_s(Q^2) = \alpha_s(p^2_{\perp min})$. Therefore, theoretical uncertainties due to the renormalization/factorization scale remain to be considered in future BFKL calculations.

There are also related experimental questions. Since the tagging jets in the BFKL calculation are single partons, the choice of the fixed cone ($R = 0.7$) jet algorithm is arbitrary. Even though the same size cone is implemented in the leading logarithmic BFKL calculation to exclude radiation within a cone around the two tagging jets, the prediction is not sensitive to the choice of cone size [10]. Experimentally the cone size is directly related to the scale of the transverse momentum for the jet, which is very important for this analysis. A better choice of the jet algorithm for low E_T jets may be the k_T algorithm [33], which is left for future analysis. Nevertheless any choice of jet algorithms will be faced with the limited detector acceptance for finding jets with a certain jet E_T threshold at the fixed center of mass energy of the Tevatron ($\sqrt{s} = 1800$ GeV). The BFKL dynamics is very sensitive to the lower E_T scale of the tagging jets. At the DØ experiment, the limited detector acceptance for additional jets with $E_T \geq 20$ GeV beyond the maximum $|\eta|$ besides the two tagging jets located at large η (≈ 3.5) may not be a problem since the limited longitudinal momentum fraction of incoming partons uses most of the energy to create radiation for the inclusive dijet system. As long as the same choice of the minimum E_T is used, comparisons between the measurement at DØ and theoretical calculations seems to be reasonable provided that the parton evolution for soft radiation below 20 GeV is fully factorized into the parton distribution functions. There is a recent argument about effects of the limited acceptance of the detector and the assumption of factorization of soft radiation beyond the allowed kinematical region [34]. Instead of tagging the two jets at extremes of rapidity, an alternative way for the measurement has been suggested to tag any combination of two jets with the same longitudinal momentum fraction for the azimuthal decorrelation.

The last question is whether the measurement of the azimuthal decorrelation is sensitive to probe BFKL dynamics at the Tevatron. One reason why predictions from parton shower Monte Carlos based on the DGLAP evolution (HERWIG and

PYTHIA) agree well with data, may be that the effect is purely kinematic in origin. Since parton shower Monte Carlos for QCD 2 by 2 processes are generally implemented with some kinematical information for higher order processes tuned with data as well as the leading logarithmic approximation in the parton showering schemes, they are more likely to reproduce the observed data. With color coherence effects including angular ordering, the two tagging jets in a parton shower Monte Carlo are likely to preserve their angular correlation even in the presence of higher order processes. In the BFKL calculation without any restriction on the phase space evolution for radiated gluons except for the infrared cutoff, however, the additional radiation is more copious and random in ϕ space so that the resultant decorrelation may be overestimated.

A better measurement to clearly probe the BFKL dynamics at the Tevatron must be free from sources of large experimental and theoretical uncertainties as well as from the kinematical constraints for the inclusive dijet production. Using data from $\sqrt{s} =$ 1800 GeV and $\sqrt{s} = 630$ GeV, the center of mass dependence of the dijet cross section is currently underway at DØ as a more direct way to explore BFKL dynamics at the Tevatron, as originally suggested by Mueller and Navelet [8]. Recently a BFKL event generator superimposing kinematical constraints for radiation between two tagging jets with the leading logarithmic BFKL calculation has also become available [35]. Imposition of kinematical constraints include the energy conservation at finite center of mass energies and the number of gluons following a Poisson distribution. At a fixed Tevatron energy, the $\sum E_T$ in a central rapidity bin is also suggested to probe BFKL dynamics.

Bibliography

[1] J.C. Collins, D.E. Soper, and G. Sterman, Nucl. Phys. **B308**, 833 (1988).

[2] L.N. Lipatov, Sov. J. Nucl. Phys. **23**, 338 (1976); E.A. Kuraev, L.N. Lipatov, and V.S. Fadin, Sov. Phys. JETP **45**, 199 (1977); Ya.Ya. Balitsky and L.N. Lipatov, Sov. J. Nucl. Phys. **28**, 822 (1978).

[3] J.E. Huth *et al.*, in Proc. of *Research Directions for the Decade, Snowmass 1990*, ed. E.L Berger (World Scientific, Singapore, 1992), p. 134.

[4] G. Altarelli and G. Parisi, Nucl. Phys. **B126**, 298 (1977); V.N. Gribov and L.N. Lipatov,Sov. J. Nucl. Phys. **15**, 78 (1972); Yu.L. Dokshitzer, Sov. Phys. JETP **73**, 1216 (1977).

[5] S.D. Ellis, Z. Kunszt, and D.E. Soper, Phys. Rev. Lett. **69**, 1496 (1992); **64**, 2121 (1990).

[6] W.T. Giele, E.W.N. Glover, and D.A. Kosower, Phys. Rev. Lett. **73**, 2019 (1994); Nucl. Phys. **B403**, 633 (1993).

[7] DØ Collaboration, V.D. Elvira, *Jet Production at DØ*, talk presented at Lathuile'97, La Thuile, March, 1997; B. Hirosky, *Inclusive Jet Production at* $\sqrt{1800}$ *GeV*, talk presented at Pheno'97, Madison, March, 1997; F. Nang, *Jet Production at the Tevatron*, talk presented at Moriond'97, Les Arcs, March, 1997.

[8] A.H. Mueller and H. Navelet, Nucl. Phys. **B282**, 727 (1987).

[9] W.J. Stirling, Nucl. Phys. **B423**, 56 (1994).

[10] V. Del Duca and C.R. Schmidt, Phys. Rev. D **51**, 2150 (1995).

[11] DØ Collaboration, S. Abachi *et al.*, Phys. Rev. Lett. **77**, 595 (1996).

[12] V. Del Duca and C.R. Schmidt, private communication.

[13] G. Marchesini and B.R. Webber, Nucl. Phys. **B310**, 461 (1988); G. Marchesini *et al.*, Comp. Phys. Comm. **67**, 465 (1992).

[14] H,-U. Bengtsson and T. Sjöstrand, Comp. Phys. Comm. **46**, 43 (1987).

[15] F. Paige and S.D. Protopopescu, BNL Report No. 38304, 1986 (unpublished).

[16] V. Del Duca and C.R. Schmidt, DESY 94-114. SCIPP 94/17, hep-ph 9407359.

[17] V. Del Duca, DESY 95-023. DFTT 13/95 (1995).

[18] A.H. Mueller, private communication.

[19] DØ Collaboration, S. Abachi *et al.*, Nucl. Instrum. Methods **A338**, 185 (1994).

[20] K. Frame and K. Fatyga, DØ internal Note 3178, (unpublished) (1997).

[21] DØ Collaboration, A. Aihara *et al.*, Nucl. Instrum. Methods Phys. Res. Sect. **A325**, 393 (1993). A. Abachi *et al.*, Nucl. Instrum. Methods Phys. Res. Sect. **A324**, 53 (1993).

[22] R. Kehoe and R. Astur, DØ Internal Note 2908, (unpublished) (1996).

[23] B. Abbott *et al.*, DØ Internal Note, in preparation.

[24] CDF Collaboration, F. Abe *et al.*, Fermilab-Pub-92 (1992).

[25] M. Bhattacharjee, J. Blazey, and B. Hirosky, DØ internal Note 2557, (unpublished) (1995).

[26] C.L. Kim, T. Heuring, and S.Y. Jun, DØ Internal Note 2477, (unpublished) (1995).

[27] A. Goussiou, S.Y. Jun, and J. Krane, Internal Note 3184, (unpublished) (1997).

[28] W. Carvalho and T. Taylor, DØ internal Note 2798, (unpublished) (1995).

[29] S.Y. Jun, DØ internal Note 3182, (unpublished) (1997).

[30] DØ Collaboration, S. Abachi *et al.*, Phys. Rev. Lett. **B357**, 500 (1995).

[31] H.L. Lai *et al.*, Phys. Rev. D **51**, 4763 (1995).

[32] V.S. Fadin and L.N. Lipatov, Nucl. Phys. **B477**, 767 (1996).

[33] S. Catani, Yu.L. Dokshitzer, M.H. Seymour, and B.R. Webber, CERN-TH-6775-93 (1993).

[34] V.T. Kim and B.B. Pivovarov, IITAP-95-01 (1995).

[35] C.R. Schmidt, MSUHEP-61217, hep-ph 9612454 (1996).